BIOCHEMISTRY
including biophysical chemistry & molecular biology

Article

pubs.acs.org/biochemistry

Understanding the Errors of SHAPE-Directed RNA Structure Modeling

Wipapat Kladwang,[†] Christopher C. VanLang,[‡] Pablo Cordero,[§] and Rhiju Das*[,†,§,∥]

Departments of [†]Biochemistry, [‡]Chemical Engineering, [§]Biomedical Informatics, and [∥]Physics, Stanford University, Stanford, California 94305, United States

Supporting Information

ABSTRACT: Single-nucleotide-resolution chemical mapping for structured RNA is being rapidly advanced by new chemistries, faster readouts, and coupling to computational algorithms. Recent tests have shown that selective 2′-hydroxyl acylation by primer extension (SHAPE) can give near-zero error rates (0−2%) in modeling the helices of RNA secondary structure. Here, we benchmark the method using six molecules for which crystallographic data are available: tRNA(phe) and 5S rRNA from *Escherichia coli*, the P4−P6 domain of the *Tetrahymena* group I ribozyme, and ligand-bound domains from riboswitches for adenine, cyclic di-GMP, and glycine. SHAPE-directed modeling of these highly structured RNAs gave an overall false negative rate (FNR) of 17% and a false discovery rate (FDR) of 21%, with at least one helix prediction error in five of the six cases. Extensive variations of data processing, normalization, and modeling parameters did not significantly mitigate modeling errors. Only one varation, filtering out data collected with deoxyinosine triphosphate during primer extension, gave a modest improvement (FNR = 12%, and FDR = 14%). The residual structure modeling errors are explained by the insufficient information content of these RNAs' SHAPE data, as evaluated by a nonparametric bootstrapping analysis. Beyond these benchmark cases, bootstrapping suggests a low level of confidence (<50%) in the majority of helices in a previously proposed SHAPE-directed model for the HIV-1 RNA genome. Thus, SHAPE-directed RNA modeling is not always unambiguous, and helix-by-helix confidence estimates, as described herein, may be critical for interpreting results from this powerful methodology.

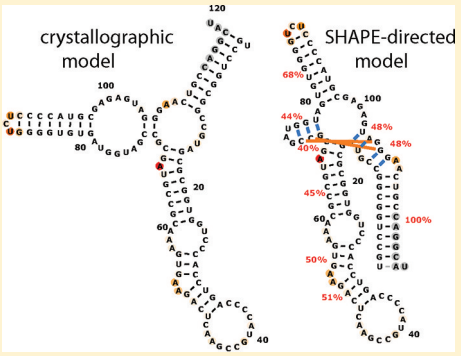

The continuing discoveries of new classes of RNA enzymes, switches, and ribonucleoprotein assemblies provide complex challenges for structural and mechanistic dissection (see, e.g., refs 1−4). While crystallographic, spectroscopic, and phylogenetic analyses have led to a deeper understanding of several key model systems, the throughput or applicability of these methods is limited, especially for noncoding RNAs that switch between multiple states in their functional cycles.[5−8] In recent years, several laboratories have revisited a widely applicable chemical approach for attaining nucleotide-resolution RNA structural information, variously called "footprinting" or "chemical structure mapping". Recent advances have included novel chemical modification strategies, faster data analysis software, accelerated readouts via capillary electrophoresis, and multiplexed purification by magnetic beads.[9−14]

Despite these advances, chemical mapping data are not expected to generally give structure models accurate at nucleotide resolution. To a first approximation, the protection of an RNA nucleotide from chemical modification indicates that it forms some interaction with a partner elsewhere in the system. However, these data by themselves do not provide enough information to define the interaction partner. Instead, the mapping data can be used to test, refine, or guide structure hypotheses derived from manual inspection or automated algorithms.[15−17] The accuracy of this approach is necessarily limited by uncertainties in the modeling, including incomplete treatment of noncanonical base pairs, base−backbone interactions, and pseudoknotted folds,[17] and imperfect correlations of chemical modification rates to structural features. Indeed, there are notable historical examples of chemical data giving misleading structural suggestions, including blind modeling work on tRNA[18,19] and 5S rRNA.[20,21]

It was therefore exciting when recent studies of 2′-OH acylation (the SHAPE method) coupled to the *RNAstructure* algorithm reported secondary structure inference with unprecedented sensitivity (98−100% helix recovery).[17] The work acknowledged several uncertainties. Measurements were taken on ribosomal RNA without protein partners, which may not form the same structures as crystallized protein-bound complexes. For other test cases, the assumed experimental structures were derived from phylogenetic analysis (P546 domain from the *bI3* group I intron), NMR data (HCV IRES), or crystals of constructs with modifications not present in the SHAPE-probed constructs ($tRNA^{Asp}$). A "gold-standard" benchmark of SHAPE-directed secondary structure inference on RNAs with corresponding crystallographic models remains unavailable. We present herein

Received: April 6, 2011
Revised: July 29, 2011
Published: August 15, 2011

SHAPE data, secondary structure inference, and analysis of systematic and statistical errors for six such RNAs containing a total of 661 nucleotides and 42 helices. Our results provide a rigorous appraisal of the strengths and limitations of this promising chemical–computational technology.

EXPERIMENTAL PROCEDURES

Preparation of Model RNAs. The DNA templates for each RNA (Table S1 of the Supporting Information) consisted of the 20-nucleotide T7 RNA polymerase promoter sequence (TTCTAATACGACTCACTATA) followed by the desired sequence. Double-stranded templates were prepared by polymerase chain reaction assembly of DNA oligomers up to 60 nucleotides in length (IDT, Integrated DNA Technologies, Coralville, IA) with Phusion DNA polymerase (Finnzymes) and purified with AMPure magnetic beads (Agencourt, Beckman Coulter) following the manufacturer's instructions. Sample concentrations were estimated on the basis of UV absorbance at 260 nm measured on Nanodrop 100 or 8000 spectrophotometers. Verification of template length was accomplished by electrophoresis of all samples and 10 and 20 bp ladder length standards (Fermentas) in 4% agarose gels (containing 0.5 mg/mL ethidium bromide) and 1× TBE (100 mM Tris, 83 mM boric acid, and 1 mM disodium EDTA).

In vitro RNA transcription reactions were conducted in 40 μL volumes with 10 pmol of DNA template, 20 units of T7 RNA polymerase (New England Biolabs), 40 mM Tris-HCl (pH 8.1), 25 mM $MgCl_2$, 2 mM spermidine, ATP, CTP, GTP, and UTP (1 mM each), 4% polyethylene glycol 1200, and 0.01% Triton X-100. Reaction mixtures were incubated at 37 °C for 4 h and monitored by electrophoresis of all samples along with 100–1000-nucleotide RNA length standards (RiboRuler, Fermentas) in 4% denaturing agarose gels [1.1% formaldehyde; run in 1× TAE (40 mM Tris, 20 mM acetic acid, and 1 mM disodium EDTA)], stained with SYBR Green II RNA gel stain (Invitrogen) following the manufacturer's instructions. RNA samples were purified with MagMax magnetic beads (Ambion), following the manufacturer's instructions, and concentrations were measured by absorbance at 260 nm on Nanodrop 100 or 8000 spectrophotometers.

Chemical Probing Measurements. Chemical modification reaction mixtures consisted of 1.2 pmol of RNA in a volume of 20 μL with 50 mM Na-HEPES (pH 8.0) and 10 mM $MgCl_2$ and/or ligand at the desired concentration (see Table S1 of the Supporting Information), and 5 μL of SHAPE modification reagent. The modification reagent was 24 mg/mL *N*-methylisatoic anhydride (NMIA) freshly dissolved in anhydrous dimethyl sulfoxide (DMSO). The reaction mixtures were incubated at 24 °C for 15–60 min, with shorter modification times for the longer RNAs to maintain overall modification rates of <30%. In control reactions (for background measurements), 5 μL of deionized water or DMSO was added instead of modification reagent, and the mixture was incubated for the same amount of time. For experiments testing DMSO effects, higher concentrations of NMIA in DMSO were prepared and 2 μL of the modification reagent was added to the 20 μL reaction mixture. Reactions were quenched with a premixed solution of 5 μL of 0.5 M Na-MES (pH 6.0), 3 μL of 5 M NaCl, 1.5 μL of oligo-dT beads [poly(A) purist (Ambion)], and 0.25 μL of 0.5 μM 5′-rhodamine-green-labeled primer (AAAAAAAAAAAAAAA-AAAAAGTTGTTGTTGTTTCTTT) complementary to the 3′ end of the RNAs (also used in our previous studies[13,14]), and 0.05 μL of a 0.5 μM Alexa-555-labeled oligonucleotide (used to verify normalization). The reaction mixtures were purified by magnetic separation, rinsed with 40 μL of 70% ethanol twice, and allowed to air-dry for 10 min while remaining on a 96-post magnetic stand. The magnetic bead mixtures were resuspended in 2.5 μL of deionized water.

The resulting mixtures of modified RNAs and primers bound to magnetic beads were reverse transcribed by the addition of a premixed solution containing 0.2 μL of SuperScript III (Invitrogen), 1.0 μL of 5× SuperScript First Strand buffer (Invitrogen), 0.4 μL of dNTPs at 10 mM each (dATP, dCTP, and dTTP, with either dGTP or dITP[22]), 0.25 μL of 0.1 M DTT, and 0.65 μL of water. The reaction mixtures (total volume of 5 μL) were incubated at 42 °C for 30 min. RNA was degraded by the addition of 5 μL of 0.4 M NaOH and incubation at 90 °C for 3 min. The solutions were neutralized by the addition of 5 μL of an acid quench (2 volumes of 5 M NaCl, 2 volumes of 2 M HCl, and 3 volumes of 3 M sodium acetate). Fluorescent DNA products were purified by magnetic bead separation, rinsed twice with 40 μL of 70% ethanol, and air-dried for 5 min. The reverse transcription products, along with magnetic beads, were resuspended in 10 μL of a solution containing 0.125 mM Na-EDTA (pH 8.0) and a Texas Red-labeled reference ladder (whose fluorescence is spectrally separated from the rhodamine green-labeled products). The products were separated by capillary electrophoresis on an ABI 3100 or ABI 3700 DNA sequencer. Reference ladders were created using an analogous protocol without chemical modification and the addition of, for example, 2′,3′-dideoxy-TTP in an amount equimolar with respect to the amount of dTTP in the reverse transcriptase reaction.

The HiTRACE software[23,24] was used to analyze the electropherograms. Briefly, traces were aligned by automatically shifting and scaling the time coordinate, based on cross correlation of the Texas Red reference ladder coloaded with all samples. Sequence assignments for bands, verified by comparison to sequencing ladders, permitted the automated peak fitting of the traces to Gaussians.

Likelihood-Based Processing of SHAPE Data. Quantified SHAPE data were corrected for attenuation of longer reverse transcriptase products due to chemical modification, normalized, and background-subtracted. Rather than using an approximate exponential correction and background scaling,[25] we used a likelihood framework to determine the final, corrected SHAPE reactivities (see also ref 26). Furthermore, a likelihood-derived analysis was implemented to average replicate SHAPE data sets across several experiments. Both of these procedures are described in detail in the methods of the Supporting Information. The algorithms are available in the functions *overmod_and_background_correct_logL.m* and *get_average_standard_state.m* within the freely available HiTRACE software package.[24] Final averaged data and errors have been made made publicly available in the Stanford RNA Mapping Database (http://rmdb.stanford.edu). The accession IDs are TRNAPH_SHP_0001, TRP4P6_SHP_0001, 5SRRNA_SHP_0001, ADDRSW_SHP_0001, CIDGMP_SHP_0001, and GLYCFN_SHP_0001.

Computational Modeling. The *Fold* executable of the RNAstructure package (version 5.3) was used to infer SHAPE-directed secondary structures. The entire RNA sequences (Table S1 of the Supporting Information), including added flanking sequences, were used for all calculations. The flag "-T 297.15" set the temperature to match our experimental conditions (24 °C). The flags "-sh", "-sm", and "-si" were used

to input the SHAPE data file, slope m, and intercept b. The latter parameters define the pseudoenergy formula $\Delta G_i = m \log(S_i + 1) + b$, where S_i is the SHAPE reactivity. In the RNAstructure implementation, these pseudoenergies are applied to each nucleotide that forms an edge base pair and doubly applied to each nucleotide that forms an internal base pair. Boltzmann probability calculations used the *partition* executable with the same flags.

Nonparametric bootstrapping analysis was conducted as follows. Given normalized SHAPE data S_i for nucleotides i = 1, 2, ..., N, a bootstrap replicate was generated by choosing N random indices i' from 1 to N, with replacement[27,28,50] (i.e., some nucleotide positions are not represented, and some are present in multiple copies; for the latter, SHAPE pseudoenergies were scaled proportionally). The resulting data sets $S_{i'}$ contained the same number of data points and carried any systematic errors present in the original data set. Secondary structure models directed by these data were analyzed in MATLAB to assess the frequency of each base pair arising in the replicates; the maximum bootstrap value across the base pairs of each helix was taken as the bootstrap value for the helix. The bootstrapping analysis is being made available on an automated server at http://rmdb.stanford.edu/structureserver.

Additional calculations were conducted with the fold() routine of the ViennaRNA package (version 1.8.4, equivalent to the "RNAfold" command lines)[29] extended to accept SHAPE data and calculate pseudoenergies with the same formula used in RNAstructure; calculations were facilitated through Python bindings available through the software's convenient SWIG (Simplified Wrapper and Interface Generator) interface. Secondary structure figures were prepared with VARNA.[30]

Assessment of Accuracy. A crystallographic helix was considered correctly recovered if more than 50% of its base pairs were observed in a helix by the computational model. (In practice, 34 of 35 such helices retained all crystallographic base pairs.) Note that, unlike prior work, helix slips of ±1 were not considered correct [i.e., the pairing (i,j) was not allowed to match the pairing $(i,j-1)$ or $(i,j+1)$].

RESULTS

Accuracy of Modeling without Experimental Data. The benchmark herein (Table S1 of Supporting Information) collects a diverse set of noncoding RNA domains, containing two classic RNA folding model systems, unmodified $tRNA^{phe}$ from *Escherichia coli*[31] and the P4–P6 domain of the *Tetrahymena* group I ribozyme;[32] a functional RNA that has been a frequent test case for modeling algorithms, *E. coli* 5S rRNA;[15,16,20,21] and three ligand-bound domains from bacterial riboswitches for adenine, cyclic di-GMP, and glycine.[33−39] For the last RNA (glycine riboswitch from *Fusobacterium nucleatum*), crystallographic data were not available at the time of modeling but released at the time of submission of the manuscript; it served as a blind test within our benchmark.

As a control, we first applied the *RNAstructure*[15,16] algorithm *Fold* without any experimental data to the benchmark set (Figure S1 of the Supporting Information). Here and below, we discuss modeling errors in terms of the false negative rate (FNR; fraction of crystallographic helices that were missed) and false discovery rate (FDR; fraction of predicted helices that were incorrect). The values are summarized, along with the related statistics of sensitivity and positive predicted value, in Table 1. To highlight features of the RNAs' global folds, we present results in terms of helices rather than individual base pairs. For the sake of completeness, FNR, FDR, sensitivity, and positive predictive values at the base pair level are also compiled in Table S2 of the Supporting Information.

Table 1. Accuracy of Secondary Structure Recovery by *RNAstructure* with and without SHAPE Data

		no. of helices[a]				
			RNAstructure		with SHAPE	
RNA	no. of nucleotides	Cryst	TP	FP	TP	FP
$tRNA^{phe}$	76	4	2	3	3	1
P4–P6 RNA	158	11	10	1	9	1
5S rRNA	118	7	1	9	6	3
adenine riboswitch	71	3	2	3	3	1
cyclic di-GMP ribosw.	80	8	6	2	6	2
glycine riboswitch	158	9	5	3	8	1
total	661	42	26	21	35	9
false negative rate[b]			38.1%		16.7%	
false discovery rate[c]			44.7%		20.5%	
sensitivity[d]			61.9%		83.3%	
positive predictive value[e]			55.3%		79.5%	

[a]Abbreviations: Cryst, number of helices in the crystallographic model; TP, true positives; FP, false positives. [b]False negative rate = 1 − TP/Cryst. [c]False discovery rate = FP/(TP + FP). [d]Sensitivity = (1 − false negative rate) = TP/Cryst. [e]Positive predictive value = (1 − false discovery rate) = TP/(TP + FP).

Without any data, the *RNAstructure* algorithm missed 16 of 42 helices, giving an FNR of 16/42 (38%). The models mispredicted an additional 21 helices, giving an FDR of 21/(26 + 21) (45%) (Table 1). These error rates are significantly worse than their ideal values (0%) and confirm the known inaccuracy of current secondary structure prediction methods without experimental guidance (see, e.g., refs 16 and 17).

Accuracy of Modeling with SHAPE Data. We then acquired SHAPE data for each RNA in 50 mM Na-HEPES (pH 8.0), 10 mM $MgCl_2$, and saturating concentrations of ligand (for the three riboswitch domains), using the modification reagent *N*-methylisatoic anhydride (NMIA). Quantitation of data for each RNA involved correction for attenuation of long products, background subtraction, and averaging of 12–28 replicates (Table S1 of the Supporting Information) guided by a likelihood framework (methods). The data were in excellent agreement with the expected structures [Figures 1 and 2 (left panels)]. Strong SHAPE reactivities occur mainly at nucleotides that are outside Watson–Crick helices observed in crystallographic models. On the basis of prior work,[17] we expected that inclusion of these data as a pseudoenergy term in the *RNAstructure* algorithm would substantially improve the accuracy of computational models, with a helix-level FNR as low as 0–2%. The improvement was indeed significant, but not to the extent expected (Figure 2, right panels; Table 1). The FNR decreased from 38 to 17% (missing 7 of 42 helices), and the FDR decreased from 45 to 21% (misprediction of 9 helices). In five of the six RNAs, the calculations failed to recover all the crystallographic helices.

Evaluating Sources of Systematic Error. The results described above give a somewhat less optimistic picture of SHAPE-directed modeling than previously published measurements.[17]

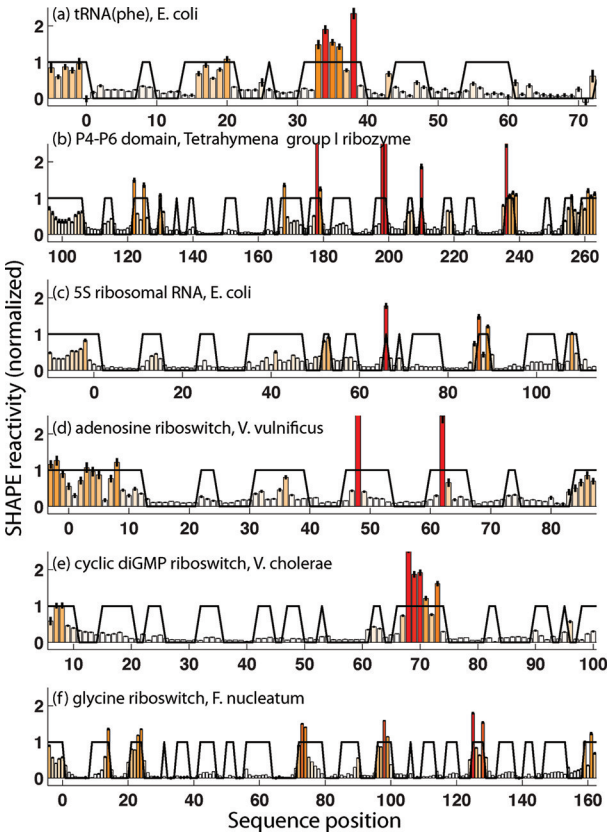

Figure 1. SHAPE reactivities measured at single-nucleotide resolution for six noncoding RNAs of known structure. Black lines mark residues that are paired or unpaired in the crystallographic secondary structures with values of 0.0 or 1.0, respectively.

The differences between SHAPE benchmarks can be most simply ascribed to different test RNAs. Nevertheless, we investigated several other possible systematic explanations for the error rates (FNR and FDR of 17 and 21%, respectively) in our test set. First, we used herein an evaluation scheme to define helix recovery more stringent than those used in previous work,[15−17] which permitted helix register slips of ±1 (see Experimental Procedures). Using those less stringent criteria gave similar FNR and FDR values of 14 and 18%, respectively. Second, we checked for experimental artifacts. Filtering out nucleotides whose SHAPE pseudoenergy errors exceeded 0.4 kcal/mol gave similar FNR and FDR values [14 and 18%, respectively (Table 2)]. Third, to test the quality of our lab's experimental procedures and data processing, we acquired SHAPE measurements on an RNA with a previously published SHAPE-directed model, the hepatitis C virus internal ribosomal entry site domain II. The resulting secondary structure (Figure S2 of the Supporting Information) agreed with prior independent work.[17] Fourth, primer extension with dNTPs containing dITP instead of dGTP reduces errors in quantitating "compressed" bands near G nucleotides[14,22,40] but gives added variance at C nucleotides due to reverse transcriptase pausing (Figure S3 of the Supporting Information and ref 14). Using only data collected with dGTP gave helix-level FNR and FDR values of 12 and 14%, respectively (Table 2), an improvement, but still higher than values of 0−2% achieved for previous test RNAs.[17] The FNR and FDR increased when we used only data collected with dITP (26 and 28%, respectively). Fifth, as an additional check on experimental artifacts, we acquired SHAPE data for all the RNAs with the newly developed 2′-OH acylating reagent 1-methyl-7-nitroisatoic anhydride (1M7);[41] the FNR and FDR for models based on these data were identical to the measurements with the more widely used NMIA (Table 2).

Sixth, model accuracy might be unduly sensitive to the highest or lowest reactivities in the SHAPE data. However, capping "outliers" (see the methods of the Supporting Information); changing the cutoffs for capping; removing outliers; only including high-reactivity data; and excluding SHAPE data for nucleotides near the 5′ and 3′ ends of the RNA did not improve the accuracy (Table 2). Seventh, the pseudoenergy for base pairing is derived from SHAPE data by a logarithmic formula [$\Delta G = m \log(1.0 + \text{SHAPE}) + b$]. Optimizing parameters m and b did not affect the FNR and improved the FDR only slightly [from 21 to 18% (Table 2)]. Eighth, choices in normalizing SHAPE data can affect the modeling, but varying the normalization by factors between 0.5- and 2-fold did not significantly improve the accuracy (Table 2). Ninth, we explored whether energy inaccuracies stem from *RNAstructure*'s thermodynamic parameters, SHAPE data, or both. Comparing energies of crystallographic and model structures indicated that both thermodynamic and SHAPE energies are imbalanced to favor incorrect models [by averages of 1.7 and 1.3 kcal/mol, respectively (Table S3 of the Supporting Information)]. Additionally, shifting the Boltzmann weight balances by increasing the modeling temperature from 24 to 37 °C did not change the error rates (Table 2). Tenth, we additionally tested for algorithm biases by recomputing models in *ViennaRNA*[29] rather than *RNAstructure*, but overall, the FNR and FDR both increased [to 26 and 28%, respectively (Table 2)].

Evidence against Crystal versus Solution Structure Discrepancies. Having found no straightforward explanation for SHAPE-directed modeling errors from systematic errors in experimental data acquisition, data processing, or modeling protocols, we investigated whether there might be differences between these RNAs' secondary structures in available crystals and under our experimental solution conditions, as occurred in prior work with extracted rRNA.[17] Several lines of evidence disfavor this hypothesis in our cases. For tRNA(phe), the P4−P6 domain, the 5S rRNA, and the purine and cyclic di-GMP riboswitch, independent crystallographic models of several variants indicate that the RNAs' secondary structures agree with phylogenetic analysis and are furthermore robust to different conditions, binding partners, and crystallographic contexts (Table S1 of the Supporting Information). In addition, while flanking sequences added to constructs (Table S1 of the Supporting Information) might disrupt the target domains, we designed these sequences to prevent such pairings and checked this lack of pairings by calculations with and without SHAPE data (Figure S1 of the Supporting Information and Figure 2).

Misfolding to kinetically trapped secondary or tertiary structures could lead to differences in solution chemical mapping data compared to those expected from crystallographic structures. To test this possibility, we acquired data for the RNAs after incubating them in 10 mM Na-MES (pH 6.0) and 10 mM $MgCl_2$ for 30 min at 50 °C (refolding conditions developed for large ribozymes[42,43]); the resulting reactivities were indistinguishable from those of RNAs without the refolding treatment (see, e.g., Figure S3 of the Supporting Information for tRNA data). Similarly, we tested for adverse effects of dimethyl sulfoxide (DMSO, used to solubilize the

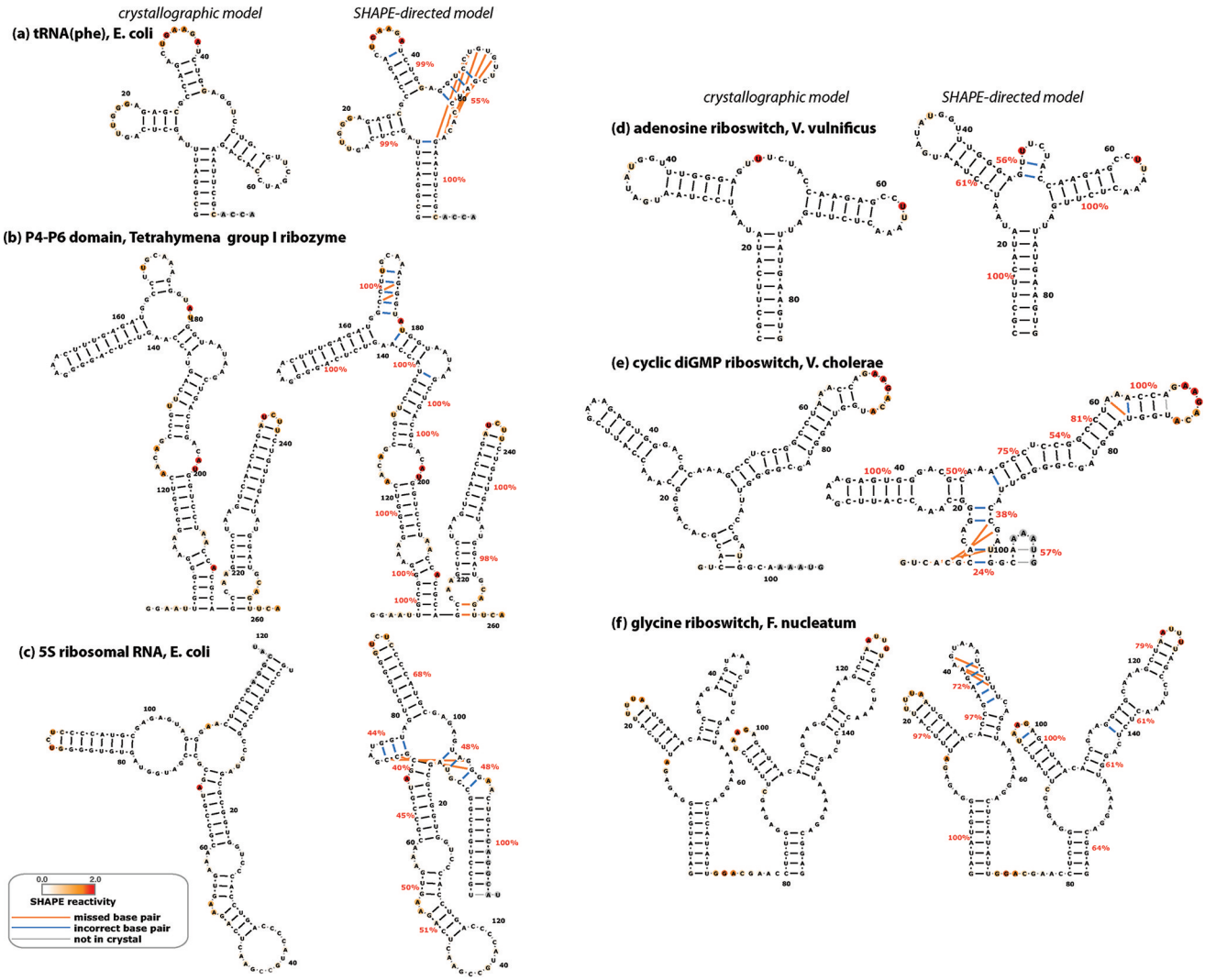

Figure 2. Crystallographic (left) and SHAPE-directed (right) secondary structure models for a benchmark of noncoding RNAs. SHAPE reactivities are shown as colors on bases and match colors in Figure 1. Cyan lines mark incorrect base pairs. Orange lines mark crystallographic base pairs missing in each model. Gray lines mark base pairs in regions outside the crystallized construct. Helix confidence estimates from bootstrap analyses are given as red percentages. For the sake of clarity, flanking sequences (see Table S1 of the Supporting Information) are not shown.

SHAPE reagent)[44] by repeating measurements at lower DMSO concentrations (10% vs 25%); SHAPE data were indistinguishable under the two conditions (Figure S3 of the Supporting Information gives tRNA data).

In addition to these results disfavoring differences in crystal and solution structures, our solution measurements gave positive evidence of the RNAs folding into the correct tertiary conformations. The P4−P6 domain and the 5S rRNA gave changes in their metal core and loop E regions, respectively, upon addition of Mg^{2+}, as expected from prior biophysical analysis (e.g., refs 45−48). The three riboswitches gave SHAPE changes with and without their ligands (Figure S4 of the Supporting Information). Most strongly, we have subjected each of these RNAs to the mutate-and-map method, a two-dimensional extension of chemical mapping,[13,14] and observed near-complete recovery of the crystallographic helices (98% sensitivity[49]), indicating that the dominant solution structure matches the structure determined by crystallography.

Assessing Information Content and Confidence by Bootstrapping. A final explanation for the errors of SHAPE-directed structure models could be that the experimental data have insufficient information content to define the secondary structure. That is, the data, while accurately reflecting each RNA's solution conformation, are also consistent with incorrect secondary structures with similar calculated energy. Indeed, the minimum energy model can be highly sensitive to small changes in the SHAPE data (see the tRNA example in Figure S5a−c of the Supporting Information), and in some cases, the incorrect lowest-energy SHAPE-directed model is within 1 kcal/mol of the crystallographic model [see $tRNA^{phe}$ and the cyclic di-GMP riboswitch (Table S3 of the Supporting Information)]. Unfortunately, quantitatively interpreting energy differences between models [as well as partition function-based base pair probabilities, which are skewed to high values (see Figure S5a of the Supporting Information)] is currently complicated by the nonphysical nature of the SHAPE pseudoenergies. For example, a useful confidence value should be a good approximation of the actual modeling accuracy. In contrast, the mean base pair probability value over all predicted helices is 88%, suggesting a false discovery rate of 12% (100% − 88%), underestimating the actual error rate of 21%.

dx.doi.org/10.1021/bi200524n | *Biochemistry* 2011, 50, 8049−8056

Table 2. Effects of Variations of Data Processing or Modeling on the Accuracy of SHAPE-Directed Secondary Structure Modeling

variation in modeling[a]	TP[b]	FP[b]	FNR (%)	FDR (%)
no SHAPE data (control)	26	21	38.1	44.7
SHAPE-directed, default parameters	**35**	**9**	**16.7**	**20.5**
remove residues with large errors[c]	36	8	14.3	18.2
use only data collected with dITP during primer extension	31	12	26.2	27.9
use only data collected with dGTP during primer extension	37	6	11.9	14.0
use 1M7 instead of NMIA reagent	35	9	16.7	20.5
cap outliers[d] at cutoff value	35	9	16.7	20.5
cap outliers[d] at 2.0	35	9	16.7	20.5
remove five additional residues from 5′ and 3′ ends	35	9	16.7	20.5
remove residues with SHAPE < 0.5	32	14	23.8	30.4
optimized m and b in pseudoenergy relation[e]	35	8	16.7	18.6
adjust normalization 2-fold	35	8	16.7	18.6
adjust normalization 1.5-fold	35	9	16.7	20.5
adjust normalization 0.75-fold	34	12	19.0	26.1
adjust normalization 0.5-fold	31	14	26.2	31.1
RNAstructure T = 37 °C (not 24 °C)	35	9	16.7	20.5
ViennaRNA[f] instead of *RNAstructure*	32	10	23.8	23.8

[a]All variations are described relative to "default conditions" (bold) using *RNAstructure* version 5.3. [b]The total number of crystallographic helices is 42. TP, true positives; FP, false positives. [c]Any residues whose estimated measurement error of SHAPE reactivity would give errors of more than ±0.4 kcal/mol if included in a base pair, using the SHAPE pseudoenergy relation. [d]Outliers were defined as in the normalization procedure: those with values above a cutoff equal to 1.5 times the interquartile range. [e]Pseudoenergy applied to base-paired nucleotides given by m log(1.0 + SHAPE) + b. Default parameters in *RNAstructure* are as follows: m = 2.6, and b = −0.8. The combinations of m and b that gave optimal accuracies for this benchmark were 3.0 and −0.6, respectively. [f]*ViennnaRNA* version 1.8.4, using the default parameter set of ref 15.

We therefore estimated the helix-by-helix confidence of SHAPE-directed models through a nonparametric bootstrapping procedure, inspired by techniques developed to evaluate phylogenetic trees from multiple-sequence alignments.[27,28,50] We generated 400 mock replicates of each data set by resampling with replacement the SHAPE data for individual residues, generating secondary structure models directed by these mock data sets, and evaluating the frequency with which each predicted helix appeared in these replicates (Figure S5b of the Supporting Information and percentage values in Figure 2). One-fourth of the modeled helices (11 of 44) appeared with bootstrap values of <55%, suggesting insufficient information for confident determination of their structure; 7 of these 11 helices were indeed incorrect. Encouragingly, the 33 helices with bootstrap values of >55% included only two errors, of which one was a single-nucleotide register shift. Further, these bootstrap values are robust to small changes in the SHAPE data (see the tRNA example in Figure S6d,e of the Supporting Information). Finally, the overall mean of the helix bootstrap values was 77%. This result predicts a false discovery rate of 23% (100% − 77%), in accord with the actual rate of 21%. Bootstrap analysis therefore appears to be well-suited for evaluating confidence in SHAPE-directed models.

Bootstrap Analysis of an Independent Test Case: The HIV-1 Genome Model. As a final demonstration of the utility of bootstrapping confidence estimation, we investigated the information content of an external data set. Recent application of the SHAPE method to the 9173-nucleotide RNA genome extracted from the NL4-3 HIV-1 virion gave a secondary structure hypothesis containing 429 helices,[51] and the quantitated SHAPE reactivity data have been published. Employing these data and previously used modeling constraints (including division of the modeled genome into five separate domains), the current version of *RNAstructure* (version 5.3) largely recovers the prior working model (Table S4 of the Supporting Information). Furthermore, bootstrapping revealed additional useful information. The 57-nucleotide 5′ TAR element, two helices with lengths greater than 10 bp in the *gag-pol* region, and the signal-peptide stem at the 5′ end of *gp120* give bootstrap values of >95%. These regions are thus high-confidence features of the SHAPE-directed model. Overall, however, 236 of 429 helices in the model have bootstrap confidence estimates of <50%. (If base pairs across the five assumed domains are permitted, more helices are found with such low bootstrap values.) The bootstrap value averaged over all predicted helices is 49%; excluding 59 stems in the prior model that are not recovered with the current version of *RNAstructure* gives a similar value of 55%. These results suggest that much of the HIV-1 secondary structure remains uncertain, even in regions that are strongly protected from SHAPE modification (Figure S7 of the Supporting Information). These low-confidence regions either form single structures that are poorly constrained by the SHAPE data or interconvert between multiple well-formed structures in solution. A tabulation of the helix-by-helix confidence estimates in Table S4 of the Supporting Information should help guide further dissection of these uncertain regions by other chemical and structural approaches.

DISCUSSION

With recent experimental and computational acceleration, nucleotide-resolution chemical mapping permits the characterization of noncoding RNAs at an unprecedented rate. Nevertheless, the resulting data are not always sufficient to determine the molecule's secondary structure, especially if additional tertiary interactions are present. The helix-level error rates found in this study of six highly structured RNAs (false negative rate and false discovery rate of 17 and 20%, respectively) are significantly better than those of models generated without data (38 and 45%, respectively) but higher than those for prior SHAPE modeling test cases (FNR of 0−2%). The modeling inaccuracy found herein is similar to error rates (FNR of ∼24%) found in benchmarks with other chemical modifiers, including dimethyl sulfate, kethoxal, and carbodiimide,[16] albeit on different RNAs and with different modeling protocols. Side-by-side tests on the same model RNAs will be necessary to rigorously compare conventional chemical approaches with SHAPE-based methods.

As with all structure characterization methods, SHAPE-directed models cannot be considered "determined structures" but instead are useful hypotheses, especially if accompanied by confidence estimates. This work proposes a bootstrapping analysis for SHAPE-directed modeling that provides such confidence values for novel RNAs. In addition to giving correct predictions for helix accuracy in six crystallized RNAs, bootstrapping analysis of the HIV-1 RNA genome finds numerous regions with high degrees of uncertainty in the RNA's current SHAPE-directed working model. More information-rich multidimensional methods, such as NMR and the mutate-and-map chemical

approaches,[13,14] should be able to test these predictions and, more generally, help attain accurate models of noncoding RNAs.

■ ASSOCIATED CONTENT

Supporting Information

Methods for likelihood-based data processing, four tables with detailed benchmark information and systematic error analyses, and eight supporting figures. This material is available free of charge via the Internet at http://pubs.acs.org.

■ AUTHOR INFORMATION

Corresponding Author

*E-mail: rhiju@stanford.edu. Phone: (650) 723-5976. Fax: (650) 723-6783.

■ ACKNOWLEDGMENTS

We thank authors of *RNAstructure* and *ViennaRNA* for making the source code freely available; M. Elazar and J. Glenn for the gift of 1M7; and J. Lucks, D. Mathews, K. Weeks, and the Das lab for comments on the manuscript.

■ REFERENCES

(1) Cruz, J. A., and Westhof, E. (2009) The dynamic landscapes of RNA architecture. *Cell 136*, 604−609.

(2) Gesteland, R. F., Cech, T. R., and Atkins, J. F. (2006) *The RNA world: The nature of modern RNA suggests a prebiotic RNA world*, Cold Spring Harbor Laboratory Press, Plainview, NY.

(3) Noller, H. F. (2005) RNA structure: Reading the ribosome. *Science 309*, 1508−1514.

(4) Pedersen, J. S., Bejerano, G., Siepel, A., Rosenbloom, K., Lindblad-Toh, K., Lander, E. S., Kent, J., Miller, W., and Haussler, D. (2006) Identification and classification of conserved RNA secondary structures in the human genome. *PLoS Comput. Biol. 2*, e33.

(5) Collins, K. (2006) The biogenesis and regulation of telomerase holoenzymes. *Nat. Rev. Mol. Cell Biol. 7*, 484−494.

(6) Staley, J. P., and Guthrie, C. (1998) Mechanical devices of the spliceosome: Motors, clocks, springs, and things. *Cell 92*, 315−326.

(7) Panning, B., Dausman, J., and Jaenisch, R. (1997) X chromosome inactivation is mediated by Xist RNA stabilization. *Cell 90*, 907−916.

(8) Winkler, W. C., and Breaker, R. R. (2003) Genetic control by metabolite-binding riboswitches. *ChemBioChem 4*, 1024−1032.

(9) Regulski, E. E., and Breaker, R. R. (2008) In-line probing analysis of riboswitches. *Methods Mol. Biol. 419*, 53−67.

(10) Wilkinson, K. A., Gorelick, R. J., Vasa, S. M., Guex, N., Rein, A., Mathews, D. H., Giddings, M. C., and Weeks, K. M. (2008) High-throughput SHAPE analysis reveals structures in HIV-1 genomic RNA strongly conserved across distinct biological states. *PLoS Biol. 6*, e96.

(11) Mitra, S., Shcherbakova, I. V., Altman, R. B., Brenowitz, M., and Laederach, A. (2008) High-throughput single-nucleotide structural mapping by capillary automated footprinting analysis. *Nucleic Acids Res. 36*, e63.

(12) Das, R., Karanicolas, J., and Baker, D. (2010) Atomic accuracy in predicting and designing noncanonical RNA structure. *Nat. Methods 7*, 291−294.

(13) Kladwang, W., and Das, R. (2010) A mutate-and-map strategy for inferring base pairs in structured nucleic acids: Proof of concept on a DNA/RNA helix. *Biochemistry 49*, 7414−7416.

(14) Kladwang, W., Cordero, P., and Das, R. (2011) A mutate-and-map strategy accurately infers the base pairs of a 35-nucleotide model RNA. *RNA 17*, 522−534.

(15) Mathews, D.H., Sabina, J., Zuker, M., and Turner, D. H. (1999) Expanded sequence dependence of thermodynamic parameters improves prediction of RNA secondary structure. *J. Mol. Biol. 288*, 911−940.

(16) Mathews, D. H., Disney, M. D., Childs, J. L., Schroeder, S. J., Zuker, M., and Turner, D. H. (2004) Incorporating chemical modification constraints into a dynamic programming algorithm for prediction of RNA secondary structure. *Proc. Natl. Acad. Sci. U.S.A. 101*, 7287−7292.

(17) Deigan, K.E., Li, T. W., Mathews, D. H., and Weeks, K. M. (2009) Accurate SHAPE-directed RNA structure determination. *Proc. Natl. Acad. Sci. U.S.A. 106*, 97−102.

(18) Levitt, M. (1969) Detailed molecular model for transfer ribonucleic acid. *Nature 224*, 759−763.

(19) Sussman, J. L., and Kim, S. (1976) Three-dimensional structure of a transfer RNA in two crystal forms. *Science 192*, 853−858.

(20) Brunel, C., Romby, P., Westhof, E., Ehresmann, C., and Ehresmann, B. (1991) Three-dimensional model of *Escherichia coli* ribosomal 5 S RNA as deduced from structure probing in solution and computer modeling. *J. Mol. Biol. 221*, 293−308.

(21) Leontis, N.B., and Westhof, E. (1998) The 5S rRNA loop E: Chemical probing and phylogenetic data versus crystal structure. *RNA 4*, 1134−1153.

(22) Mills, D. R., and Kramer, F. R. (1979) Structure-independent nucleotide sequence analysis. *Proc. Natl. Acad. Sci. U.S.A. 76*, 2232−2235.

(23) Das, R., Laederach, A., Pearlman, S. M., Herschlag, D., and Altman, R. B. (2005) SAFA: Semi-automated footprinting analysis software for high-throughput quantification of nucleic acid footprinting experiments. *RNA 11*, 344−354.

(24) Yoon, S., Kim, J., Hum, J., Kim, H., Park, S., Kladwang, W., and Das, R. (2011) HiTRACE: High-Throughput Robust Analysis for Capillary Electropherograms. *Bioinformatics 27*, 1798−1805.

(25) Vasa, S. M., Guex, N., Wilkinson, K. A., Weeks, K. M., and Giddings, M. C. (2008) ShapeFinder: A software system for high-throughput quantitative analysis of nucleic acid reactivity information resolved by capillary electrophoresis. *RNA 14*, 1979−1990.

(26) Aviran, S., Trapnell, C., Lucks, J. B., Mortimer, S. A., Luo, S., Schroth, G. P., Doudna, J. A., Arkin, A. P., and Pachter, L. (2011) Modeling and automation of sequencing-based characterization of RNA structure. *Proc. Natl. Acad. Sci. U.S.A. 108*, 11069−11074.

(27) Efron, B., and Tibshirani, R. J. (1998) *An Introduction to the Bootstrap*, Chapman & Hall, Boca Raton, FL.

(28) Efron, B., Halloran, E., and Holmes, S. (1996) Bootstrap confidence levels for phylogenetic trees. *Proc. Natl. Acad. Sci. U.S.A. 93*, 13429−13434.

(29) Hofacker, I. L. (2004) RNA secondary structure analysis using the Vienna RNA package. *Current Protocols in Bioinformatics*, Chapter 12, Unit 12, p 12, Wiley, New York.

(30) Darty, K., Denise, A., and Ponty, Y. (2009) VARNA: Interactive drawing and editing of the RNA secondary structure. *Bioinformatics 25*, 1974−1975.

(31) Byrne, R. T., Konevega, A. L., Rodnina, M. V., and Antson, A. A. (2010) The crystal structure of unmodified tRNAPhe from *Escherichia coli*. *Nucleic Acids Res. 38*, 4154−4162.

(32) Cate, J. H., Gooding, A. R., Podell, E., Zhou, K., Golden, B. L., Kundrot, C. E., Cech, T. R., and Doudna, J. A. (1996) Crystal structure of a group I ribozyme domain: Principles of RNA packing. *Science 273*, 1678−1685.

(33) Mandal, M., and Breaker, R. R. (2004) Adenine riboswitches and gene activation by disruption of a transcription terminator. *Nat. Struct. Mol. Biol. 11*, 29−35.

(34) Serganov, A., Yuan, Y. R., Pikovskaya, O., Polonskaia, A., Malinina, L., Phan, A. T., Hobartner, C., Micura, R., Breaker, R. R., and Patel, D. J. (2004) Structural basis for discriminative regulation of gene expression by adenine- and guanine-sensing mRNAs. *Chem. Biol. 11*, 1729−1741.

(35) Sudarsan, N., Lee, E. R., Weinberg, Z., Moy, R. H., Kim, J. N., Link, K. H., and Breaker, R. R. (2008) Riboswitches in eubacteria sense the second messenger cyclic di-GMP. *Science 321*, 411−413.

(36) Kulshina, N., Baird, N. J., and Ferre-D'Amare, A. R. (2009) Recognition of the bacterial second messenger cyclic diguanylate by its cognate riboswitch. *Nat. Struct. Mol. Biol. 16*, 1212−1217.

(37) Smith, K. D., Lipchock, S. V., Livingston, A. L., Shanahan, C. A., and Strobel, S. A. (2010) Structural and biochemical determinants of ligand binding by the c-di-GMP riboswitch. *Biochemistry 49*, 7351−7359.

(38) Mandal, M., Lee, M., Barrick, J. E., Weinberg, Z., Emilsson, G. M., Ruzzo, W. L., and Breaker, R. R. (2004) A glycine-dependent riboswitch that uses cooperative binding to control gene expression. *Science 306*, 275−279.

(39) Butler, E. B., Xiong, Y., Wang, J., and Strobel, S. A. (2011) Structural basis of cooperative ligand binding by the glycine riboswitch. *Chem. Biol. 18*, 293−298.

(40) Wilkinson, K. A., Merino, E. J., and Weeks, K. M. (2006) Selective 2′-hydroxyl acylation analyzed by primer extension (SHAPE): Quantitative RNA structure analysis at single nucleotide resolution. *Nat. Protoc. 1*, 1610−1616.

(41) Mortimer, S. A., and Weeks, K. M. (2007) A fast-acting reagent for accurate analysis of RNA secondary and tertiary structure by SHAPE chemistry. *J. Am. Chem. Soc. 129*, 4144−4145.

(42) Russell, R., and Herschlag, D. (1999) New pathways in folding of the *Tetrahymena* group I RNA enzyme. *J. Mol. Biol. 291*, 1155−1167.

(43) Russell, R., Das, R., Suh, H., Travers, K. J., Laederach, A., Engelhardt, M. A., and Herschlag, D. (2006) The paradoxical behavior of a highly structured misfolded intermediate in RNA folding. *J. Mol. Biol. 363*, 531−544.

(44) Hickey, D. R., and Turner, D. H. (1985) Solvent effects on the stability of A7U7p. *Biochemistry 24*, 2086−2094.

(45) Takamoto, K., Das, R., He, Q., Doniach, S., Brenowitz, M., Herschlag, D., and Chance, M. R. (2004) Principles of RNA compaction: Insights from the equilibrium folding pathway of the P4-P6 RNA domain in monovalent cations. *J. Mol. Biol. 343*, 1195−1206.

(46) Correll, C. C., Freeborn, B., Moore, P. B., and Steitz, T. A. (1997) Metals, motifs, and recognition in the crystal structure of a 5S rRNA domain. *Cell 91*, 705−712.

(47) Lemay, J. F., Penedo, J. C., Tremblay, R., Lilley, D. M., and Lafontaine, D. A. (2006) Folding of the adenine riboswitch. *Chem. Biol. 13*, 857−868.

(48) Kwon, M., and Strobel, S. A. (2008) Chemical basis of glycine riboswitch cooperativity. *RNA 14*, 25−34.

(49) Kladwang, W., VanLang, C. C., Cordero, P., and Das, R. (2011) Two-dimensional chemical mapping for non-coding RNAs: The mutate-and-map strategy. *Nat. Chem.*, in revision.

(50) Felsenstein, J. (1985) Confidence limits on phylogenies: An approach using the bootstrap. *Evolution 39*, 783−791.

(51) Watts, J. M., Dang, K. K., Gorelick, R. J., Leonard, C. W., Bess, J. W. Jr., Swanstrom, R., Burch, C. L., and Weeks, K. M. (2009) Architecture and secondary structure of an entire HIV-1 RNA genome. *Nature 460*, 711−716.

Supporting Information for: Understanding the errors of SHAPE-directed RNA structure modeling

Wipapat Kladwang[1], Christopher C. VanLang[2], Pablo Cordero[3], and Rhiju Das[1,3,4]*

Departments of Biochemistry[1], Chemical Engineering[2], Biomedical Informatics[3], and Physics[4], Stanford University, Stanford CA 94305

** To whom correspondence should be addressed: rhiju@stanford.edu. Phone: (650) 723-5976. Fax: (650) 723-6783.*

This document contains the following Supporting Information:

Supporting Methods

Likelihood-based attenuation correction, background subtraction, and normalization of SHAPE data

Quantified SHAPE data were corrected for attenuation of longer reverse transcriptase products due to chemical modification, normalized, and background-subtracted. This procedure involved optimization carried out over three parameters, the overall modification rate γ, a normalization factor for the data α, and a scaling for the background β, defined and estimated as follows. First, let y_i be the observed fraction of products stopping at each nucleotide $i = 1, 2, \ldots N$ in the reverse transcription reaction, ordered so that longer (attenuated) products have larger indices i; and define $y_{N+1} = 1 - \sum_{i=1}^{N} y_i$ be the fraction of products that are fully extended. These probabilities are equal to the underlying stopping probabilities p_i times the product of probabilities that the reverse transcriptase has not stopped earlier:

$$y_i = p_i \prod_{j=1}^{i-1} (1 - p_j) \,, \quad (1)$$

which can be inverted by recursively calculating $p_1 = y_1$, then $p_2 = y_2(1-p_1)^{-1}$, then $p_3 = y_3(1-p_1)^{-1}(1-p_2)^{-1}$, etc. For convenience, define $c_i = p_i/y_i$ as an attenuation correction factor. [In the limit that the y_i are approximately constant and much smaller than 1, the solution reduces to an exponential fall-off $c_i^{-1} = \exp[-\langle y_i \rangle i]$, as was effectively assumed in (*1*, *2*), but this approximation is unnecessary.]

Fluorescence measurements of reverse transcription products from capillary electrophoresis detectors are in arbitrary units; evaluating (1) requires that the y_i be

properly normalized, and this is in principle achieved by the constraint that $\sum_{i=1}^{N} y_i + y_{N+1} = 1$. However, in practice, the intensity of the longest products (e.g., y_{N+1}) cannot measured precisely. The strong fluorescence of these fully extended products typically saturates the experimental detector. Thus, the values y_i are defined only up to a proportionality constant γ, i.e., $y_i = \gamma s_i / S_i$ where s_i are the observed fluorescence intensities and $S = \sum_{j=1}^{N_{observed}} s_j$; we need to select amongst γ < 1.

We estimate γ at the same time as the two other unknown proportionality constants in the data normalization and background subtraction. Let b_i be the quantified band intensities from control measurements (no SHAPE reaction), which we assume require negligible correction from attenuation. The background-subtracted SHAPE reactivities are given in terms of unknown constants α and β by:

$$s_i^{\text{correct}} = \alpha[p_i - \beta b_i] = \alpha[c_i(\gamma) s_i - \beta b_i] \quad (2)$$

We then optimized the log-likelihood function:

$$L = \prod_{i=1}^{n} \alpha c_i(\gamma) \exp\left[F(\alpha[c_i(\gamma) s_i - \beta b_i])\right] \quad (3)$$

Here, F was chosen as a piecewise linear function that (i) gives an exponential distribution of positive SHAPE reactivities [similar to what is empirically observed (SI Fig. S8)], (ii) penalizes negative SHAPE reactivities, and (iii) results in a convex optimization problem for maximum likelihood estimation. The functional form was $F(x) = F_+(x - x_0)$ if $x > x_0$, and $F(x) = -F_-(x - x_0)$ if $x \leq x_0$. The parameters $F_+ = 5.0$, $F_- = 25.0$, and $x_0 = 0.06$ were used, and this formulation appears robust: varying F_+ and F_- by

two-fold, changing x_0 to zero, or using a double exponential fit for $x > x_0$, did not change the resulting corrected data beyond experimental errors (as estimated in the next section). We optimized (3) by performing a grid search of $\zeta = \gamma/(1-\gamma)$ from 0.0 to 2.0 in 0.05 increments and iteratively solving for α and then β (through relations obtained by $dL/d\alpha = 0$ and $dL/d\beta = 0$) until convergence. Applying the maximum likelihood values of α, β, and γ in (2) gave the corrected SHAPE reactivities. The algorithm is available in the function *overmod_and_background_correct_logL.m* within the freely available HiTRACE software package (*3*).

Averaging across replicates, estimation of errors, and normalization

The acquisition of multiple replicates across several experiments permitted high-quality final averaged data $\overline{S}_i$ with error estimates $\overline{\sigma}_i$. To carry out the averaging, we noted that individual experiments might have different levels of measurement precision, and the variance of measurements within each experiment provide an estimate of that precision. These estimates, however, do not include systematic errors that differ between experiments, e.g., differing fluorescent backgrounds in different capillary electrophoresis instruments. We therefore carried out a two-part averaging. First, the data within each experiment $j = 1, 2, .. M$ were averaged to give S_i^j and σ_i^j. As an example, suppose we have available 20 replicate measurements of each background/overmodification-corrected SHAPE profile s_i^k, where $k = 1$ to 20. Suppose these data were measured for 4 independently prepared RNAs across $M = 5$ different days/experiments. Then each k is the member of one and only one of 5 subsets E_j. Let N_j be the number of RNAs in set E_j (here $N_j = 4$). For $j = 1, 2, \ldots 5$,

$$S_i^j = \frac{1}{N_j} \sum_{k \in S_j} s_i^k \tag{4}$$

The estimated errors for these SHAPE data are:

$$\sigma_i^j = \left(\frac{1}{N_j} \sum_{k \in S_j} \left[s_i^k - S_i^j \right]^2 \right)^{1/2} \tag{5}$$

To combine measurements across multiple experiments, these merged data were averaged, with the inclusion of a position-dependent scale-factor α_i that accounts for additional sources of experiment-to-experiment error. Explicitly, the assumed likelihood model was:

$$L(S_i) = \prod_j \frac{1}{2\pi\alpha_i\sigma_i^j} e^{-\left(S_i - S_i^j\right)^2 \Big/ 2\left(\alpha_i \sigma_i^j\right)^2} \tag{6}$$

This gives maximum-likelihood combined signal values $\overline{S}_i$ and final Gaussian errors $\overline{\sigma}_i$ of:

$$\overline{S}_i = \frac{\sum_j \left[S_i^j / \left(\sigma_i^j\right)^2 \right]}{\sum_j \left[1 / \left(\sigma_i^j\right)^2 \right]} \tag{7}$$

$$\overline{\sigma}_i = \alpha_i \left(\sum_j \left[1 / \left(\sigma_i^j\right)^2 \right] \right)^{-1/2} .$$

Here, α_i is a scale factor and is again determined by optimizing the likelihood:

$$\alpha_i = \frac{1}{M}\sum_{j=1}^{M}\left[\left(\overline{s_i} - s_i^j\right)^2 / \left(\sigma_i^j\right)^2\right] \quad (8)$$

In practice, to obtain a robust estimate of this error scale factor, the average in (8) is taken across a 5-nucleotide window of bands around each nucleotide *i*. An example of this averaging is given in SI Fig. S3. These data, averaged across multiple replicates, were then normalized following a previously described procedure that was found to be optimal for *E. coli* ribosomal RNA (*1*). Briefly, the data sets were divided by a normalization factor, determined as the average of the top tenth percentile of band intensities. 'Outliers', identified as band intensities that exceeded 1.5 times the interquartile range, were removed before determining this factor. The resulting values lie mostly between 0 and 2 (see e.g., main text Fig. 1). The overall algorithm is available in the function *get_average_standard_state.m* within the freely available HiTRACE software package (*3*).

Table S1. Benchmark for SHAPE-directed secondary structure modeling.

RNA, source	Solution conditions[a]	Replicates[b]	Expts[b]	Offset[c]	PDB[d]	Sequence & Secondary Structure[e]
tRNA^{phe}, *E. coli*	Standard	14	7	-15	**1L0U** 1EHZ	ggaacaaacaaaacaGCGGAUUUAGCUCAGUUGGGAGAGCGCCAGACUGAAGAUCUG GAGGUCCUGUGUUCGAUCCACAGAAUUCGCACCAaaaccaaagaaacaacaacaaca ac .....((((((..((((........)))).((((.........)))).....(((((.......))))))))))..... ..
P4-P6 domain, *Tetrahymena* ribozyme	Standard[f]	28	11	89	**1GID** 1L8V 1HR2 2R8S	ggccaaaacaacgGAAUUGCGGGAAAGGGGUCAACAGCCGUUCAGUACCAAGUCUCA GGGGAAACUUUGAGAUGGCCUUGCAAAGGGUAUGGUAAUAAGCUGACGGACAUGGUC CUAACCACGCAGCCAAGUCCUAAGUCAACAGAUCUUCUGUUGAUAUGGAUGCAGUUC Aaaaccaaaccaaagaaacaacaacaacaac .....(((((...((((((.....(((.((((.(((..(((((((((....)))))))))..((.......))....)))......)))))))....))))))..)).)))))(...(((...(((((((((...)))))))))..))))...)).. .....
5S rRNA, *E. coli*	Standard	12	6	-20	**3OFC** 3OAS 3ORB 2WWQ …	ggaaaggaaagggaaagaaaUGCCUGGCGGCCGUAGCGCGGUGGUCCCACCUGACCC CAUGCCGAACUCAGAAGUGAAACGCCGUAGCGCCGAUGGUAGUGUGGGGUCUCCCCA UGCGAGAGUAGGGAACUGCCAGGCAUaaaacaaaacaaagaaacaacaacaacaac .....(((((((((.....(((((((....(((((((... .....)))).))...)))...)))))).)).((.......(((((((...)))))))).......)).))))))))..... .....
Adenine riboswitch, *V. vulnificus* (*add*)	Standard + 5 mM adenine	19	6	-8	**1Y26** 1Y27 2G9C 3GO2 …	ggaaaggaaagggaaagaaaCGCUUCAUAUAAUCCUAAUGAUAUGGUUUGGGAGUUU CUACCAAGAGCCUUAAACUCUUGAUUAUGAAGUGaaaacaaaacaaagaaacaacaa caacaac .....(((((((((...((((((.........)))))).... ....((((((.......))))))..))))))))..... .....
c-di-GMP riboswitch, *V. cholerae* (*VC1722*)	Standard + 10 μM cyclic di-guanosine mono-phosphate	15	6	0	**3MXH** 3IWN 3MUV 3MUT …	ggaaaaauGUCACGCACAGGGCAAACCAUUCGAAAGAGUGGGACGCAAAGCCUCCGG CCUAAACCAGAAGACAUGGUAGGUAGCGGGGUUACCGAUGGCAAAAUGcauacaaac caaagaaacaacaacaacaac .....((((.....((...((((((....))))))...))...(((.((((((((..((.........)))))))..))))))...)).))..... .....
Glycine riboswitch, *F. nucleatum*	Standard + 10 mM glycine	22	8	-10	**3P49**	ggacagagagGAUAUGAGGAGAGAUUUCAUUUUAAUGAAACACCGAAGAAGUAAAUC UUUCAGGUAAAAAGGACUCAUAUUGGACGAACCUCUGGAGAGCUUAUCUAAGAGAUA ACACCGAAGGAGCAAAGCUAAUUUUAGCCUAAACUCUCAGGUAAAAGGACGGAGaaaa acacaacaaagaaacaacaacaacaac .....(((((((.....(((((....)))))).(((....(((.....)))...)))........)))))))).....(((((.....((((.....))))).(((...(((((.....(((....))).....))))..)))).....)))))... .....

[a] Standard conditions are: 10 mM $MgCl_2$, 50 mM Na-HEPES, pH 8.0 at 24 °C.

[b] All data average over experiments carried out on at least four different days to minimize systematic errors in sample preparations; within each experiment, two or more independently prepared and purified RNA stocks were assayed.

[c] Number added to sequence index to yield numbering used in previous biophysical studies, and in Figs. 1 and 2 of the main text.

[d] The first listed PDB ID was the source of the assumed crystallographic secondary structure; other listed IDs contain sequence variants, different complexes, or different crystallographic space groups and confirm this structure.

[e] In the sequence, lowercase symbols denote 5´and 3´ buffer sequences, including primer binding site (last 20 nucleotides). In all cases, designs were checked in RNAstructure and ViennaRNA to give negligible base pairing between added sequences and target domain. Structure is given in dot-bracket notation, and here denotes Watson/Crick base pairs for which there is crystallographic evidence. Only helices with two or more base pairs are included. For the adenine riboswitch, a two-base-pair helix [25-50, 26-49] that is not nested in the given secondary structure and involved in an extensive non-canonical loop-loop interaction is not included.

[f] Additional measurements were carried out with 30% methylpentanediol (MPD) due to reports that its presence in crystallization buffer can change SHAPE reactivity of the P4-P6 RNA (*4*). Measurements with MPD (10 replicates) gave different reactivities in the P5abc region; final SHAPE-directed secondary structure models mispredicted an additional helix compared to models guided by no-MPD data.

Table S2. Base-pair-level statistics of secondary structure recovery by *RNAstructure* with and without SHAPE data. TP=true positives; FP=false positives. TP´and FP´ are the same, but allowing matches of base pair (i,j) with (i±1, j±1).

RNA	Len.	Number of base pairs								
		Cryst[a]	RNAstructure				+ SHAPE			
			TP	FP	TP´	FP´	TP	FP	TP´	FP´
$tRNA^{phe}$	76	20	12	12	12	12	15	6	15	4
P4-P6 RNA	158	48	44	9	48	2	44	7	46	2
5S rRNA	118	34	9	31	9	31	32	7	32	7
Adenine ribosw.	71	21	15	10	15	10	21	2	21	2
c-di-GMP ribosw.	80	25	21	5	21	3	21	6	21	4
Glycine riboswitch	158	40	23	18	23	16	37	7	37	5
Total	661	188	124	85	128	74	170	35	172	24
False negative rate[b]			34.0%		31.9%		9.6%		8.5%	
False discovery rate[c]			40.7%		36.6%		17.1%		12.2%	
Sensitivity[d]			66.0%		68.1%		90.4%		91.5%	
Positive predictive value[e]			59.3%		63.4%		82.9%		87.8%	

[a] Cryst = number of helices in crystallographic model.
[b] False negative rate = 1 - TP/Cryst.
[c] False discovery rate = FP/(TP+FP).
[d] Sensitivity = (1 - false negative rate) = TP/Cryst.
[e] Positive predictive value = (1 - false discovery rate) = TP/(TP+FP).

Table S3. Sources of poor discrimination of correct from incorrect secondary structures. Thermodynamic energies of base pairs and SHAPE pseudoenergies in kcal/mol, calculated in *RNAstructure*.

	SHAPE-directed model			Crystallographic model[a]			Difference[b]		
RNA	E_{total}	E_{thermo}	E_{SHAPE}	E_{total}	E_{thermo}	E_{SHAPE}	E_{total}	E_{thermo}	E_{SHAPE}
$tRNA^{phe}$	-40.1	-20.3	-19.8	-39.6	-20.5	-19.1	-0.5	0.2	-0.7
P4-P6	-125.6	-54.8	-70.8	-114.9	-46.4	-68.5	-10.7	-8.4	-2.3
5S rRNA	-95.5	-47.5	-48.0	-91.9	-45.7	-46.2	-3.6	-1.8	-1.8
Ade ribosw.	-48.2	-16.6	-31.6	-48.2	-16.6	-31.6	0.0	0.0	0.0
c-di-GMP ribosw.	-63.6	-26.3	-37.3	-62.7	-26.4	-36.3	-0.9	0.1	-1.0
Gly. ribosw.	-98.5	-24.8	-73.7	-96	-24.5	-71.5	-2.5	-0.3	-2.2
Average	-78.5	-31.7	-46.9	-75.5	-30.0	-45.5	-3.0	-1.7	-1.3

[a] For a fair comparison to the SHAPE-directed model, this is the lowest energy secondary structure produced by *RNAstructure* with the same SHAPE data, but forced to contain the crystallographically observed base pairs. For the adenine riboswitch, an 'extra' two-base-pair helix appears in this structure.
[b] Negative values indicate inaccuracy in structure discrimination.
[c] E_{total} and E_{thermo} are derived from from *efn2* (the *RNAstructure* package) run with and without SHAPE data, respectively. E_{SHAPE} is the difference of the two values.

Table S4. Helix-by-helix bootstrap confidence estimates for the SHAPE-directed model of the HIV-1 RNA genome. Models were generated by applying RNAstructure 5.3 to SHAPE data from ref. (*5*). Following prior work, the temperature was set to the default (37 °C); slope *m* and intercept *b* of SHAPE pseudoenergy relation were set to 3.0 kcal/mol and -0.6 kcal/mol, respectively; maximum sequence distance between base pairs was set to 600; modeling was carried out for separate subsegments 1-2844, 2836-5722, 5676-6832, 6807-7791, and 7779-9173; and positions at termini of these subsegments (2836-2845, 5676-5724, 6799-6838, 7779-7791, 9171-9173) and in pseudoknotted regions (179-216, bound to tRNALys primer; 255-263 in the dimerization loop DIS; and 74-86 and 408-375, forming the 5´ polyA signal) were forced to remain unpaired. "BP1", "BP2", and "len" give two residues marking the starting base pair of each stem and stem length; "P(boot)" and "BPP" are bootstrap confidence value and maximum Boltzmann probability in the stem as percentages; and "Modeled" gives whether the stem was in the working model of (*5*) and recovered with RNAstructure 5.3 (Y) or not (N), or whether the stem is newly predicted herein (X). Continued on next two pages.

BP1	BP2	len	P(boot)	BPP	Modeled	BP1	BP2	len	P(boot)	BPP	Modeled	BP1	BP2	len	P(boot)	BPP	Modeled
1	57	3	95.5	31.1	Y[a]	1214	1247	5	89	99.8	Y	2619	2666	4	96.5	100	Y
5	54	11	100	100	Y[a]	1223	1239	6	94	100	Y	2625	2661	4	91.5	98.9	Y
17	43	5	100	100	Y[a]	1249	1263	4	88.5	99.9	Y	2629	2654	10	100	100	Y
25	38	4	100	100	Y[a]	1350	1727	2	17	2.4	Y	2667	2686	3	47	6.5	Y
58	104	8	99.5	100	Y	1353	1724	5	20.5	2.8	Y	2671	2683	3	41	5.8	Y
67	94	3	99.5	100	Y	1360	1394	4	19.5	2	Y	2727	2745	4	89	100	Y
70	90	4	99.5	100	Y	1375	1387	5	69.5	95.3	Y	2731	2740	2	76	95.2	Y
106	343	9	40	98.5	Y	1396	1558	4	37	5.5	Y	2781	2802	7	92	100	Y
125	223	7	26.5	95.4	Y	1401	1554	3	38	5.6	Y	2811	2835	2	67	98.8	Y
134	178	8	77.5	99.4	Y	1405	1414	2	24	24.5	Y	2814	2833	6	80.5	100	Y
143	167	2	51.5	93.2	Y	1418	1457	3	29.5	21.8	Y	2846	3381	6	68.5	65.8	Y
146	164	2	64.5	94	Y	1421	1443	7	92.5	99.7	Y	2852	3374	5	53	64.6	Y
148	160	3	79	99.7	Y	1459	1522	6	54	29.4	Y	2876	3273	5	10.5	22.1	Y
228	334	6	11	27.1	Y	1465	1515	3	37.5	26.4	Y	2892	3176	5	16	22.4	Y
236	282	3	70	69.3	Y	1469	1511	3	34	26.2	Y	2908	3160	4	12.5	21.2	Y
243	277	4	93	77.2	Y	1477	1504	3	18.5	20.9	Y	2925	3129	3	7.5	17.5	Y
248	270	7	100	100	Y	1481	1500	4	14.5	15.6	Y	2939	3088	5	2.5	7.9	Y
283	299	3	37	70	Y	1531	1541	3	69.5	90.7	Y	2946	2953	2	22.5	18.1	Y
286	295	3	34.5	69.3	Y	1568	1707	10	100	100	Y[B]	2972	3038	5	8	8.5	Y
312	325	5	98	100	Y	1583	1694	3	53.5	68.3	Y[B]	2995	3006	4	38.5	46.6	Y
363	750	5	4.5	1.6	Y	1590	1683	6	48.5	77.8	Y[B]	3015	3023	3	28	45.9	Y
399	484	9	98	100	Y	1598	1640	2	35.5	65.8	Y[B]	3040	3058	3	36	56.1	Y
501	526	6	33	87	Y	1604	1636	8	78	98.7	Y[B]	3044	3055	2	35	55.9	Y
510	518	2	22	62	Y	1615	1625	3	97	100	Y[B]	3089	3105	2	24.5	17.7	Y
582	657	2	41.5	68.2	Y	1645	1672	12	100	100	Y[B]	3093	3101	3	41	38	Y
586	652	8	66.5	99.7	Y	1760	1785	4	27.5	28.4	Y	3140	3149	3	60.5	81	Y
595	625	4	58.5	91.6	Y	1767	1779	2	30	27.2	Y	3178	3190	3	40.5	91	Y
599	616	5	93	99.8	Y	1813	1916	6	53	94.9	Y	3205	3223	3	93	99.4	Y
628	636	3	36.5	83.8	Y	1823	1849	6	66	90.9	Y	3243	3256	4	50.5	47.1	Y
678	741	4	4	4.4	Y	1829	1842	3	88.5	99.4	Y	3285	3334	1	7	17.7	Y
683	691	2	25.5	12.1	Y	1862	1881	5	78	99.9	Y	3287	3332	6	15.5	22.7	Y
693	722	6	73.5	99.6	Y	1991	2326	9	57.5	100	Y	3297	3322	5	34	25.9	Y
702	714	2	59	93.4	Y	2015	2121	8	99.5	100	Y	3336	3358	5	8.5	25.4	Y
752	1172	5	22	36.9	Y	2024	2112	10	99	100	Y	3344	3351	2	9.5	22.3	Y
795	849	9	87.5	99.9	Y	2042	2070	7	82	99.9	Y	3393	3402	2	19	11.7	Y
821	831	4	88	98.2	Y	2051	2062	3	35	56.3	Y	3404	3943	4	11.5	5	Y
871	913	2	56	84.1	Y	2072	2082	3	25.5	23.3	Y	3410	3936	4	15.5	32.1	Y
874	911	6	77	99.3	Y	2135	2144	3	35.5	82.6	Y	3414	3931	7	18.5	33.8	Y
921	964	5	51	99.1	Y	2145	2171	6	58	91.6	Y	3423	3924	4	12	31.7	Y
926	935	3	20.5	68.1	Y	2201	2238	7	38.5	89.8	Y	3427	3496	4	16	37	Y
946	957	2	30	68.5	Y	2245	2260	4	35	91.5	Y	3432	3439	2	35	53.8	Y
1028	1064	5	67	82.2	Y	2268	2310	5	88	100	Y	3458	3468	3	44.5	89.4	Y
1076	1100	3	99	99.9	Y	2273	2301	5	88	99.8	Y	3497	3917	5	15	39.3	Y
1080	1097	5	100	100	Y	2279	2296	1	88	49.4	Y	3523	3653	6	15.5	5.6	Y
1102	1142	5	85	99.6	Y	2378	2429	8	68	99.2	Y	3532	3644	2	8	4	Y
1110	1137	3	84	99.9	Y	2391	2421	3	32	69.7	Y	3535	3550	3	31	53.5	Y
1116	1132	6	75	98.8	Y	2547	2778	9	52	0	Y	3581	3593	4	11	3.8	Y
1177	1312	5	64.5	39.2	Y	2558	2576	3	16	1.7	Y	3606	3639	2	19	41.4	Y
1183	1306	5	68.5	39.2	Y	2596	2712	5	31.5	0.4	Y	3609	3636	6	25	50.7	Y
1193	1299	6	83	99.2	Y	2603	2705	4	30.5	0.4	Y	3692	3907	6	18	61.6	Y
1214	1247	5	89	99.8	Y	2619	2666	4	96.5	100	Y	3699	3800	4	35	84.9	Y
1223	1239	6	94	100	Y	2625	2661	4	91.5	98.9	Y	3704	3759	7	94	99.9	Y
1249	1263	4	88.5	99.9	Y	2629	2654	10	100	100	Y	3818	3899	9	89.5	100	Y
1350	1727	2	17	2.4	Y	2667	2686	3	47	6.5	Y	3840	3890	6	91	100	Y
1353	1724	5	20.5	2.8	Y	2671	2683	3	41	5.8	Y	3857	3872	4	82.5	99.8	Y

[a] 5´ TAR element.
[b] gag-pol region.

BP1	BP2	len	P(boot)	BPP	Modeled	BP1	BP2	len	P(boot)	BPP	Modeled	BP1	BP2	len	P(boot)	BPP	Modeled
4204	4349	8	96.5	100	Y	5499	5519	3	47	79.8	Y	6538	6595	4	66	95	Y
4280	4299	4	91.5	96.8	Y	5503	5515	4	40	75.7	Y	6543	6590	3	45	33.4	Y
4301	4316	4	32.5	28.6	Y	5530	5581	5	24.5	69.1	Y	6546	6586	6	96	100	Y
4362	4503	7	45.5	52.4	Y	5536	5576	3	27	69.5	Y	6552	6579	4	90.5	99.7	Y
4447	4488	4	44	40.8	Y	5542	5571	2	31.5	70.5	Y	6618	6635	4	21.5	59.7	Y
4456	4479	2	34	31.5	Y	5545	5568	3	36	72.5	Y	6623	6630	2	18.5	56.4	Y
4458	4473	3	56	55.8	Y	5549	5565	2	15	49.1	Y	6706	6762	2	26	43.1	Y
4490	4496	2	32	36	Y	5600	5644	2	59.5	61.4	Y	6711	6757	9	90	100	Y
4551	5036	10	81	100	Y	5605	5639	6	95	100	Y	6839	7188	4	52	79.7	Y
4573	4586	4	26.5	53.3	Y	5612	5632	1	95	76.9	Y	6846	7179	2	71	97.1	Y
4588	4934	9	71	99.9	Y	5614	5631	4	95	99.9	Y	6850	7176	5	88	99.7	Y
4601	4914	8	87	100	Y	5725	6314	3	27.5	25.2	Y	6864	7113	5	10.5	16.8	Y
4614	4902	2	16	24.3	Y	5745	6243	10	97	99.9	Y	6870	6886	6	26	30.7	Y
4642	4674	3	28	85.4	Y	5763	6147	4	15.5	12.1	Y	6893	7077	1	19	7.9	Y
4646	4670	4	35	94.4	Y	5770	6142	6	37.5	16.9	Y	6894	7075	1	20	7.2	Y
4694	4732	3	31.5	86.2	Y	5793	6013	7	96.5	100	Y	6895	7073	7	97.5	100	Y
4698	4728	4	31.5	86.4	Y	5803	6004	5	91.5	99.9	Y	6904	7056	10	98	100	Y
4754	4770	6	100	100	Y	5816	5830	6	98.5	100	Y	6923	7040	4	78	97.9	Y
4797	4899	7	97.5	100	Y	5846	5861	6	98.5	100	Y[c]	6938	6956	5	81.5	96.8	Y
4807	4822	3	99.5	100	Y	5867	5997	7	94	100	Y	6964	6973	3	33.5	66.3	Y
4829	4891	9	100	100	Y	5874	5989	5	93.5	99.9	Y	6983	7016	3	13.5	33.9	Y
4840	4856	6	100	100	Y	5887	5894	2	26.5	63.6	Y	6988	7009	2	34.5	70.7	Y
4938	4999	6	81	100	Y	5896	5980	6	57.5	89.9	Y	6991	7007	4	40	80.5	Y
4951	4985	5	75.5	99.9	Y	5904	5913	2	36.5	63.6	Y	7079	7099	7	94	100	Y
4960	4980	6	99.5	100	Y	5915	5973	3	21	46.9	Y	7114	7136	7	94	98.9	Y
5010	5022	4	39.5	92.6	Y	5927	5962	4	24	41.4	Y	7150	7170	5	13	16.8	Y
5070	5100	6	19	47.2	Y	5931	5952	4	69	99.5	Y	7245	7599	1	66.5	80	Y
5083	5094	4	51	87.8	Y	5936	5947	4	78.5	100	Y	7247	7597	5	84	99.9	Y
5114	5132	4	73.5	4.8	Y	6024	6135	3	19.5	4.2	Y	7256	7590	8	99	100	Y
5139	5675	2	10	0.9	Y	6048	6066	5	67.5	92.4	Y	7272	7578	11	99.5	100	Y
5143	5673	7	20.5	1.7	Y	6072	6125	3	13	2.4	Y	7283	7566	3	99	100	Y
5154	5204	4	43	57.5	Y	6076	6121	2	12.5	2.4	Y	7291	7557	7	98.5	100	Y
5166	5194	5	75.5	85.2	Y	6078	6118	2	15.5	2.5	Y	7305	7538	7	94.5	100	Y
5206	5396	2	29	40.6	Y	6083	6113	3	22	4.5	Y	7312	7530	3	94	100	Y
5209	5394	5	77	100	Y	6092	6102	3	6.5	3.6	Y	7316	7526	5	94	100	Y
5216	5384	8	82	100	Y	6149	6159	2	2	5.4	Y	7321	7520	4	99.5	99.9	Y
5234	5265	3	29	56.9	Y	6185	6200	2	40.5	15.5	Y	7325	7515	4	99.5	100	Y
5239	5261	5	69	98.7	Y	6270	6290	6	69	98	Y	7333	7508	4	100	100	Y
5267	5297	6	65.5	97.9	Y	6328	6798	3	35.5	30.6	Y	7337	7503	5	100	100	Y
5273	5283	4	52	82.1	Y	6332	6375	6	20	34.8	Y	7343	7408	6	92.5	100	Y
5303	5343	4	50.5	96.6	Y	6381	6780	4	16	46.1	Y	7350	7378	1	67	95.5	Y
5307	5337	4	40	94.7	Y	6385	6775	3	15	47.7	Y	7353	7375	3	77	100	Y
5311	5331	6	76.5	98.1	Y	6393	6767	2	13	44.3	Y	7356	7371	2	82	100	Y
5349	5370	2	17	32.1	Y	6398	6704	5	30.5	88.6	Y	7358	7368	4	94.5	100	Y
5352	5367	1	17	20.1	Y	6416	6695	4	25	86.3	Y	7383	7399	6	100	100	Y
5355	5364	3	26	43	Y	6421	6521	8	26.5	85.8	Y	7411	7428	5	78	99.5	Y
5404	5419	5	99	100	Y	6432	6513	6	28	84.5	Y	7438	7464	3	63.5	98.1	Y
5425	5438	3	32.5	52.5	Y	6456	6467	4	41	88.4	Y	7443	7459	7	78	99.5	Y
5440	5450	3	28.5	40.4	Y	6475	6497	5	18	36.7	Y	7468	7493	9	100	100	Y
5473	5650	5	1	2.3	Y	6536	6598	2	39.5	67.5	Y	7601	7616	4	29	58.2	Y
5499	5519	3	47	79.8	Y	6538	6595	4	66	95	Y	7627	7636	2	48.5	58.4	Y
5503	5515	4	40	75.7	Y	6543	6590	3	45	33.4	Y	7647	7692	6	59.5	81.6	Y
5530	5581	5	24.5	69.1	Y	6546	6586	6	96	100	Y	7705	7770	6	67.5	99.8	Y
5536	5576	3	27	69.5	Y	6552	6579	4	90.5	99.7	Y	7712	7764	2	58	73.9	Y
5542	5571	2	31.5	70.5	Y	6618	6635	4	21.5	59.7	Y	7716	7760	2	61	96.4	Y

[c]signal-peptide stem at 5′end of gp120.

BP1	BP2	len	P(boot)	BPP	Modeled	BP1	BP2	len	P(boot)	BPP	Modeled	BP1	BP2	len	P(boot)	BPP	Modeled
7939	8107	2	13.5	76.6	Y	1341	1795	2	1.5	0.1	N	383	393	2	18.5	25.9	X
7941	8051	2	12	24.3	Y	1346	1790	4	1	0	N	380	396	2	14.5	17.6	X
7944	8049	5	50	97.8	Y	1729	1757	6	15	18.3	N	533	549	4	31	38.2	X
7949	8043	3	45	97.3	Y	1737	1749	3	26.5	21.4	N	972	979	2	17.5	4.6	X
7954	8039	3	19.5	31.9	Y	1796	1946	7	23.5	0.8	N	968	983	3	17.5	4.4	X
7969	8024	4	39	89.8	Y	1809	1920	2	20.5	2	N	966	984	2	8	1.7	X
7991	8015	5	94.5	100	Y	1811	1917	1	27.5	2.1	N	993	999	2	5	1.3	X
7997	8009	3	72	98.3	Y	1922	1930	3	29.5	18.2	N	987	1008	5	9	1.7	X
8053	8077	5	43	66.5	Y	1948	2545	7	7	0	N	770	1014	4	14	3.1	X
8059	8071	3	65.5	98.6	Y	2328	2348	3	17	1.7	N	765	1019	4	13.5	3	X
8083	8099	3	7.5	26.2	Y	2333	2343	3	17.5	1.6	N	761	1027	3	14.5	3.1	X
8169	8205	4	33.5	80.1	Y	2352	2520	8	7	0.5	N	1731	1752	5	40.5	74	X
8173	8194	3	38.5	64.4	Y	2363	2376	4	20.5	2.3	N	1795	1920	5	3.5	0.4	X
8309	8326	2	69	8.3	Y	2432	2484	6	30.5	1.1	N	1787	1925	3	3	0.3	X
8648	8667	3	45.5	66.1	Y	2448	2472	4	29.5	1.1	N	1345	1930	3	8.5	0	X
8651	8663	4	67.5	99.8	Y	2486	2497	2	2.5	0.2	N	2350	2357	2	19.5	35.8	X
8669	8679	3	98	100	Y	2714	2725	4	20	20.2	N	2348	2360	2	15	25.1	X
8686	9009	7	19	5.9	Y	3945	4518	4	7	0	N	2343	2366	5	17	47.2	X
8694	8999	4	12	5.7	Y	3958	3970	4	12.5	33.2	N	2430	2436	2	38	72.8	X
8700	8803	6	44.5	99	Y	4057	4068	2	31	24.5	N	1941	2453	13	51	0.1	X
8723	8751	11	96	100	Y	4539	5135	3	7.5	0	N	2496	2513	2	67.5	90.6	X
8753	8773	8	98.5	100	Y	7540	7546	2	22.5	43.4	N	2492	2517	3	65.5	92.3	X
8779	8790	3	34.5	81.8	Y	7638	7778	4	6.5	1.7	N	2477	2531	4	20	13.2	X
8807	8994	6	13	5.8	Y	7644	7774	3	3.5	0.6	N	2469	2544	8	37	17	X
8817	8985	5	31	6	Y	8226	8268	5	1	0	N	2721	2750	4	35	43	X
8830	8973	4	35	5.8	Y	8275	8348	5	26.5	3.8	N	2899	3167	3	5.5	9.8	X
8838	8965	2	21	4.7	Y	8282	8341	5	51	4.5	N	3765	3773	2	16.5	26.8	X
8851	8859	2	25	10.1	Y	8290	8308	3	19	1.7	N	3961	3970	2	5.5	19.6	X
8867	8906	10	99.5	100	Y	8358	8684	5	0.5	0.1	N	3958	4047	2	5.5	9	X
8878	8896	4	99	100	Y	8371	8412	1	5	1.1	N	3945	4058	4	11.5	30.8	X
8884	8890	1	98	91.6	Y	8373	8411	6	12.5	6.3	N	4131	4518	2	22	0.4	X
8912	8927	5	69.5	87.2	Y	8379	8404	1	11.5	4.1	N	6251	6258	2	24	65.6	X
9042	9057	5	84.5	99.7	Y	8382	8401	2	10.5	4.5	N	6390	6770	2	12.5	21.2	X
9059	9067	2	77	96.2	Y	8417	8641	7	3	77.2	N	7156	7164	2	13	13.4	X
9074	9134	5	98	99.9	Y	8432	8528	4	8	65.8	N	7621	7643	3	19	37.9	X
9080	9129	11	100	100	Y	8440	8519	3	9.5	58.9	N	7236	7777	4	47.5	95.9	X
9092	9118	5	100	100	Y	8455	8505	3	13	48.7	N	8265	8277	4	44.5	92.6	X
9100	9113	4	100	100	Y	8461	8498	11	28.5	62.6	N	8288	8339	6	39.5	1.1	X
9141	9170	4	76	70.6	Y	8530	8631	2	4	74.1	N	8282	8348	5	35.5	1.5	X
9145	9165	5	76	70.7	Y	8533	8628	10	16.5	89.3	N	8424	8435	3	14.5	17	X
382	537	4	6	40.5	N	8546	8617	4	8	54.9	N	8418	8442	4	28	12.7	X
547	565	4	37.5	58.5	N	8551	8565	3	6.5	60.4	N	8469	8478	2	14	6	X
760	1010	4	15	75.7	N	8578	8597	3	14.5	88.7	N	8465	8482	3	6.5	3	X
765	1005	2	15	75.5	N	8840	8935	2	1.5	0.2	N	8408	8493	6	10	5.7	X
769	1001	5	16	75.7	N	8845	8932	4	13	4.8	N	8406	8496	2	8.5	5.7	X
855	994	2	1.5	39.1	N	8949	8961	3	55	95.3	N	8404	8499	2	8.5	5.7	X
915	970	3	4	20.2	N	9011	9139	5	6.5	0	N	8398	8505	4	9	5.7	X
979	991	5	34.5	65.3	N	9020	9037	4	6.5	0	N	8392	8511	2	9	5.1	X
1026	1068	2	42	80	N	9025	9033	2	6.5	0	N	8370	8534	8	32	11	X
1200	1206	2	24.5	28.5	N	187	197	3	43	98.8	X	8367	8537	2	34.5	9.3	X
1341	1795	2	1.5	0.1	N	383	393	2	18.5	25.9	X	8358	8546	8	45	10.3	X
1346	1790	4	1	0	N	380	396	2	14.5	17.6	X	8228	8551	5	26	1.8	X
1729	1757	6	15	18.3	N	533	549	4	31	38.2	X	8224	8555	3	26	1.7	X
1737	1749	3	26.5	21.4	N	972	979	2	17.5	4.6	X	8596	8619	2	22	0.4	X
1796	1946	7	23.5	0.8	N	968	983	3	17.5	4.4	X	8591	8624	2	18	0.6	X

Figure S1. *RNAstructure* secondary structure models for a benchmark of six structured RNAs. Cyan lines mark incorrect base pairs; orange lines mark crystallographic base pairs missing in each model. (Figure is in two parts.)

(a) tRNA(phe), E. coli

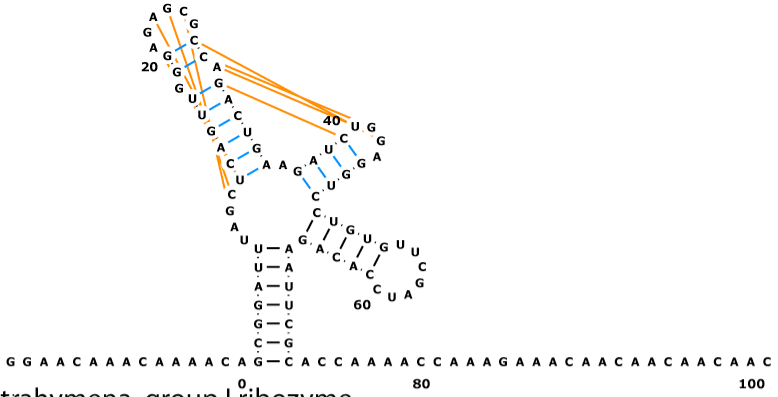

(b) P4-P6 domain, Tetrahymena group I ribozyme

(c) 5S ribosomal RNA, E. coli

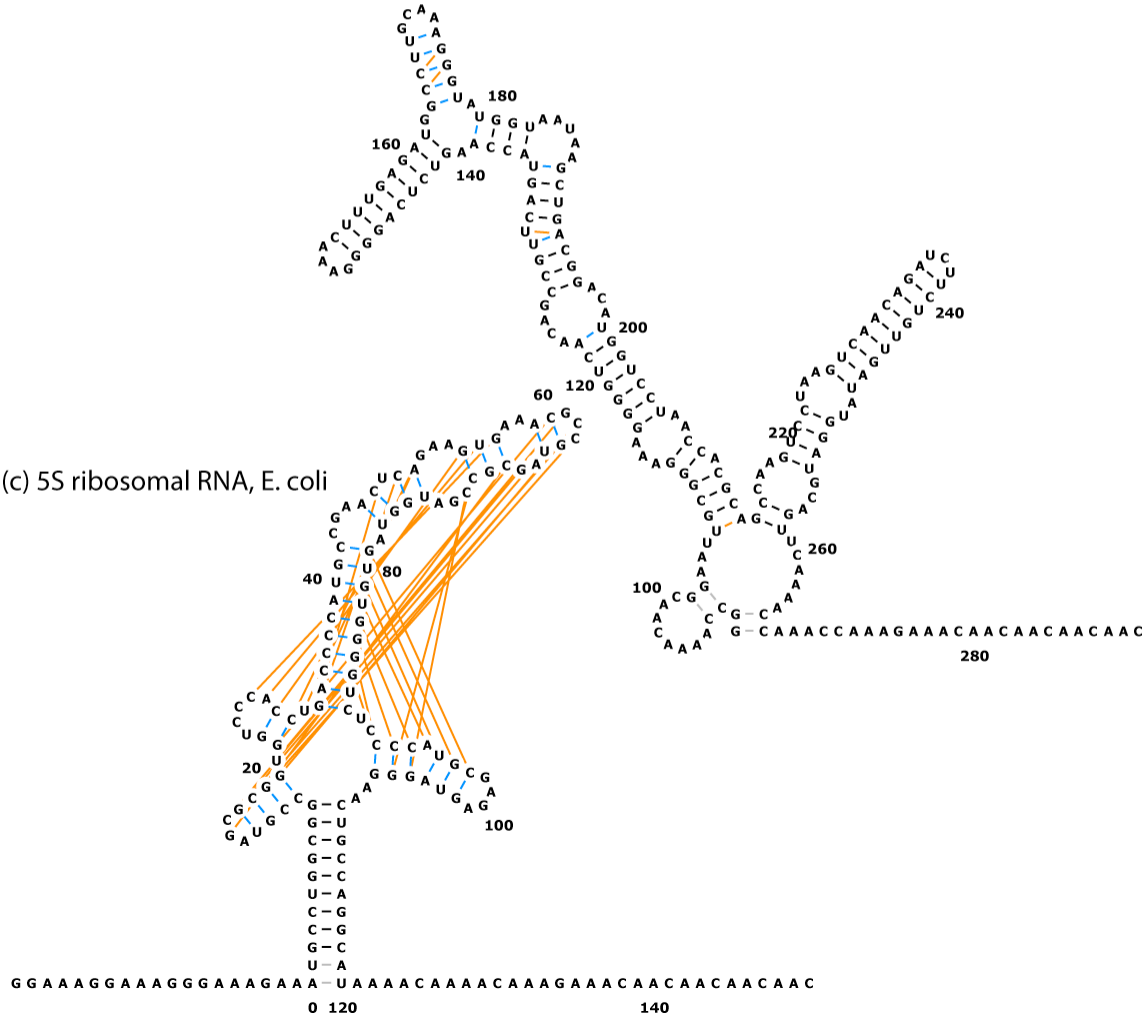

(d) adenosine riboswitch, V. vulnificus

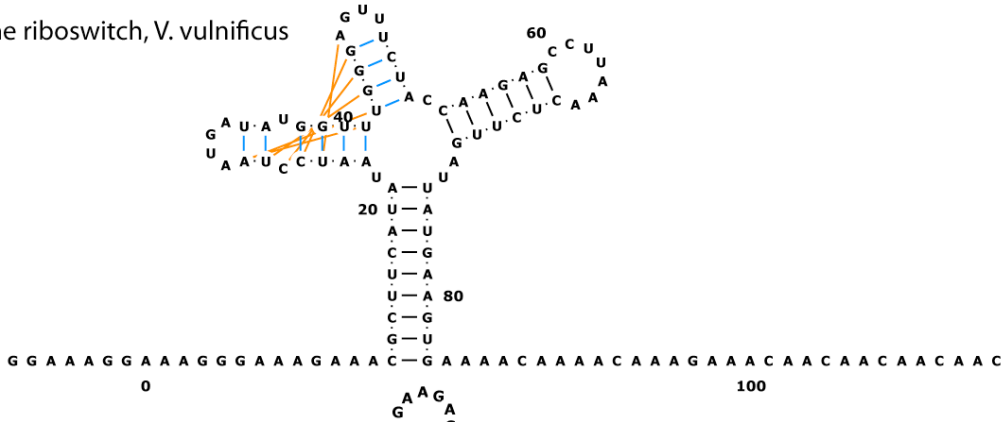

(e) cyclic diGMP riboswitch, V. cholerae

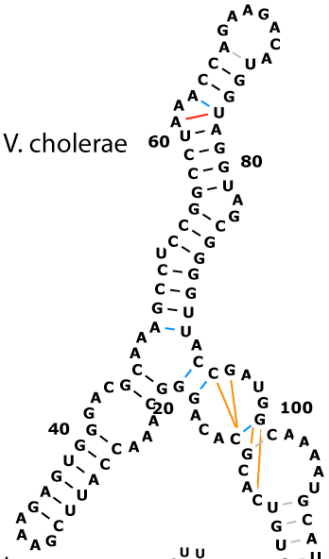

(f) glycine riboswitch, F. nucleatum

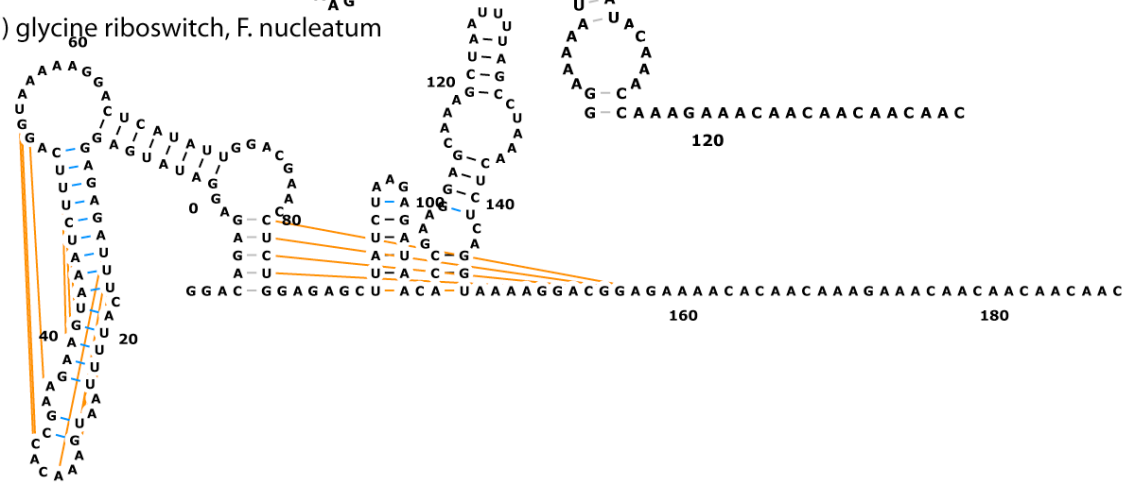

Figure S2. Recovery of SHAPE-directed model for a previously studied HCV RNA. As a control, SHAPE data were collected herein for the hepatitis C virus internal ribosomal entry site (HCV IRES) domain II; the resulting SHAPE-directed model agrees with prior work (*1*) and phylogenetic and NMR analyses [see, e.g., (*6*)]. Model is colored by SHAPE reactivity (see color scalebar). Helix confidence estimates from bootstrap analyses (see main text) are given as red percentage values. Flanking sequences (similar to those added to benchmark RNAs) are shown in gray.

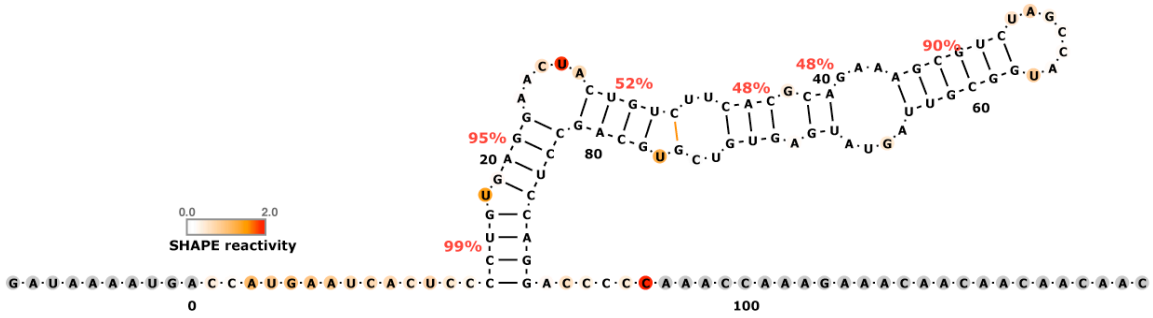

Figure S3. SHAPE data acquired with different dNTP mix for primer extension, refolding prior to chemical modification, and different DMSO backgrounds. Colored error bars and lines give background-subtracted data for $tRNA^{phe}$ (*E. coli*) from six experiments: two experiments in which the dATP, dCTP, dITP, and dTTP were used for reverse transcription of modified RNA; and four experiments in which standard dATP, dCTP, dGTP, and dTTP were used. Each experiment involved at least two replicate measurements; error bars represent standard deviations within each experiment. Arrows mark high-variance bands at C nucleotides in dITP experiments (red) due to poor incorporation of dITP, and near G nucleotides in dGTP experiments (blue) due to band compression. 'Refold' experiment 5 (green) involved incubation of RNA at 10 mM $MgCl_2$, 10 mM Na-MES, pH 6.0 at 50 °C for thirty minutes and gave reactivities indistinguishable from conditions without incubation. Low DMSO experiment 6 (dark green) contained 10% DMSO during chemical modification and gave reactivities indistinguishable from conditions used for other experiments (25% DMSO). Black error bars and lines gives the final averaged SHAPE reactivity averaged over all experiments, taking into account the estimated errors (see SI Methods).

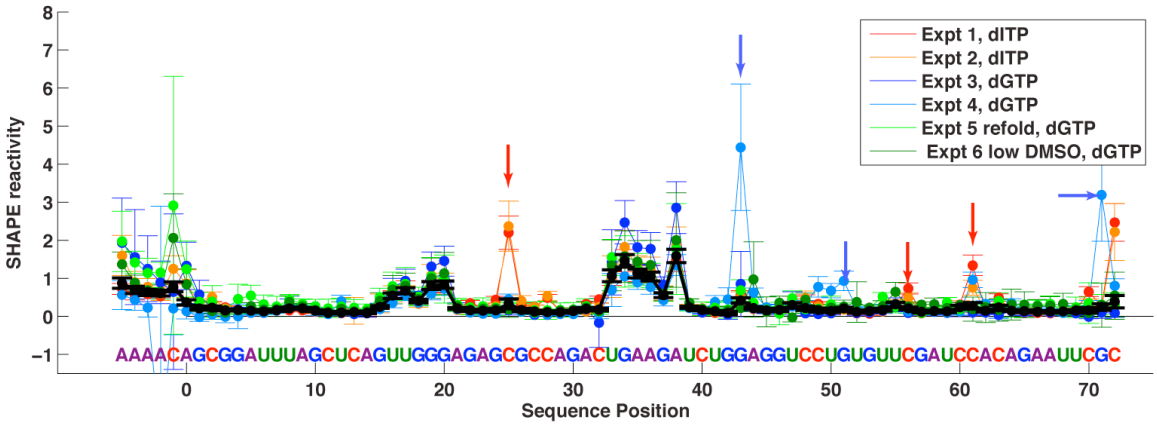

Figure S4. Demonstration that solution SHAPE data reflect folded or ligand-bound conformations. Significant differences were observed upon addition of 10 mM $MgCl_2$ with a background of 50 mM Na-HEPES (for the P4-P6 domain & 5S rRNA) and upon addition of ligand with a background of 10 mM $MgCl_2$, 50 mM Na-HEPES, pH 8.0 (for the ligand-binding domains of riboswitches for adenine, c-di-GMP, and glycine). Regions that become protected upon Mg^{2+}-induced tertiary folding or ligand binding are annotated on the data, and compare well to expectations from previous biophysical and crystallographic studies (*7-13*).

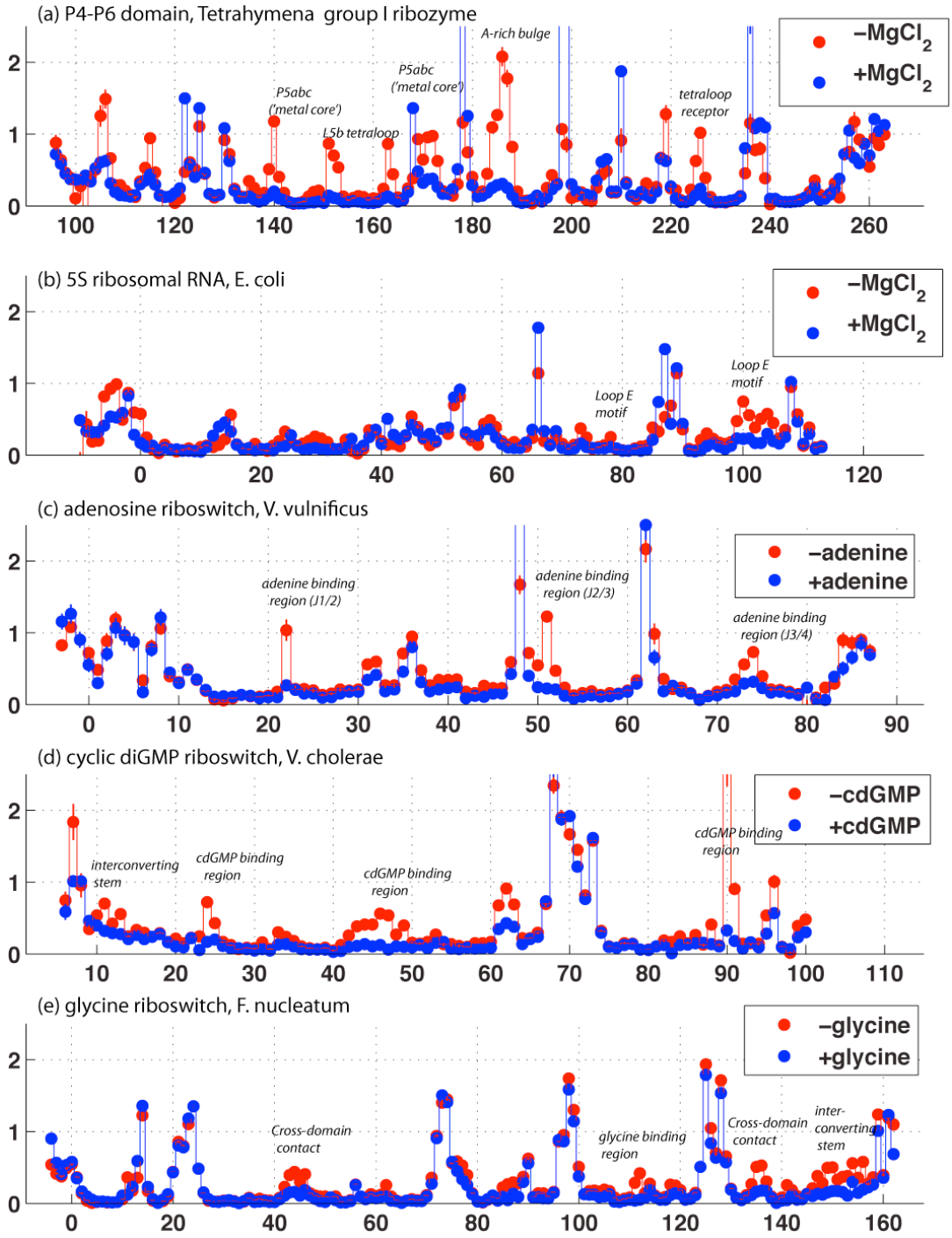

Figure S5. Partition-function and bootstrap analysis of SHAPE-directed secondary structure models. A confidence estimate for each helix in each of the six benchmark SHAPE-directed models was determined by (1) partition-function-based Boltzmann probabilities and (2) a nonparametric bootstrap analysis (repeating the modeling with 'replicate' data sets generated by randomly resampling the data with replacement). The confidence estimates for the two analyses correlate approximately, but partition function probabilities are skewed to higher values than bootstrap probabilities. Helices that agree (blue) or disagree (red) with crystallographic secondary structures are plotted separately. Dashed lines mark 80% and 55% separatrix values, above which two incorrect helices are observed, and 29 and 31 correct helices are observed for Boltzmann probability and bootstrap analyses, respectively.

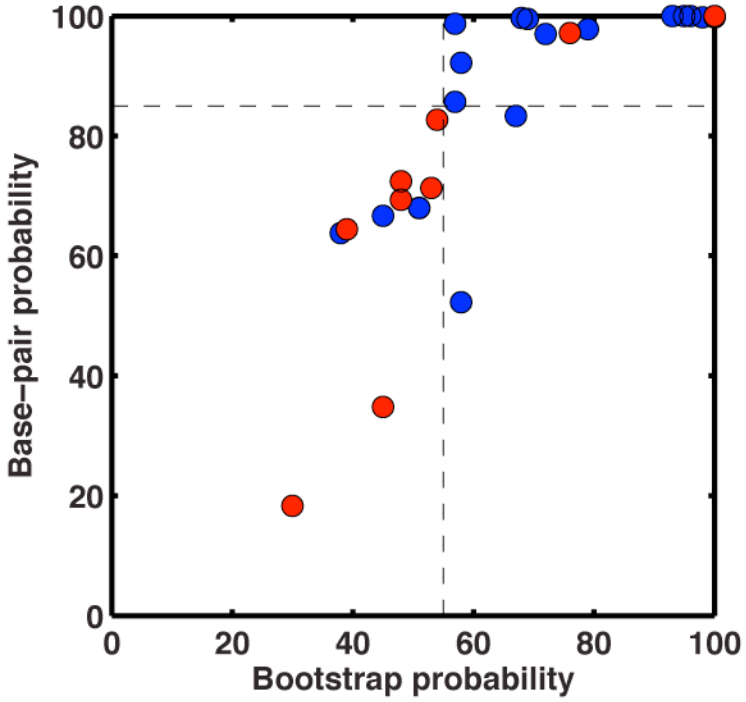

Figure S6. Sensitivity of minimum-energy model and robustness of bootstrap values to small changes in tRNA SHAPE data. (a) Comparison of SHAPE data sets obtained by averaging over all collected data (14 replicates; blue) and by averaging over just those data collected with primer extension with standard deoxynucleotide triphosphates (no dITP; i.e., dATP, dCTP, dGTP, dTTP) (6 replicates; red). (b,c) Minimum-energy SHAPE-directed secondary structures are different for the two data sets in the pairings of the third helix; bootstrap values given as red percentage values. (d,e) Helix probabilities from bootstrap analysis shown in grayscale, with 0 to 100% shown as white to black. Bootstrap values at alternate locations of third helix are shown as red percentage values; they are similar for the two data sets. Red squares mark crystallographic base pairs.

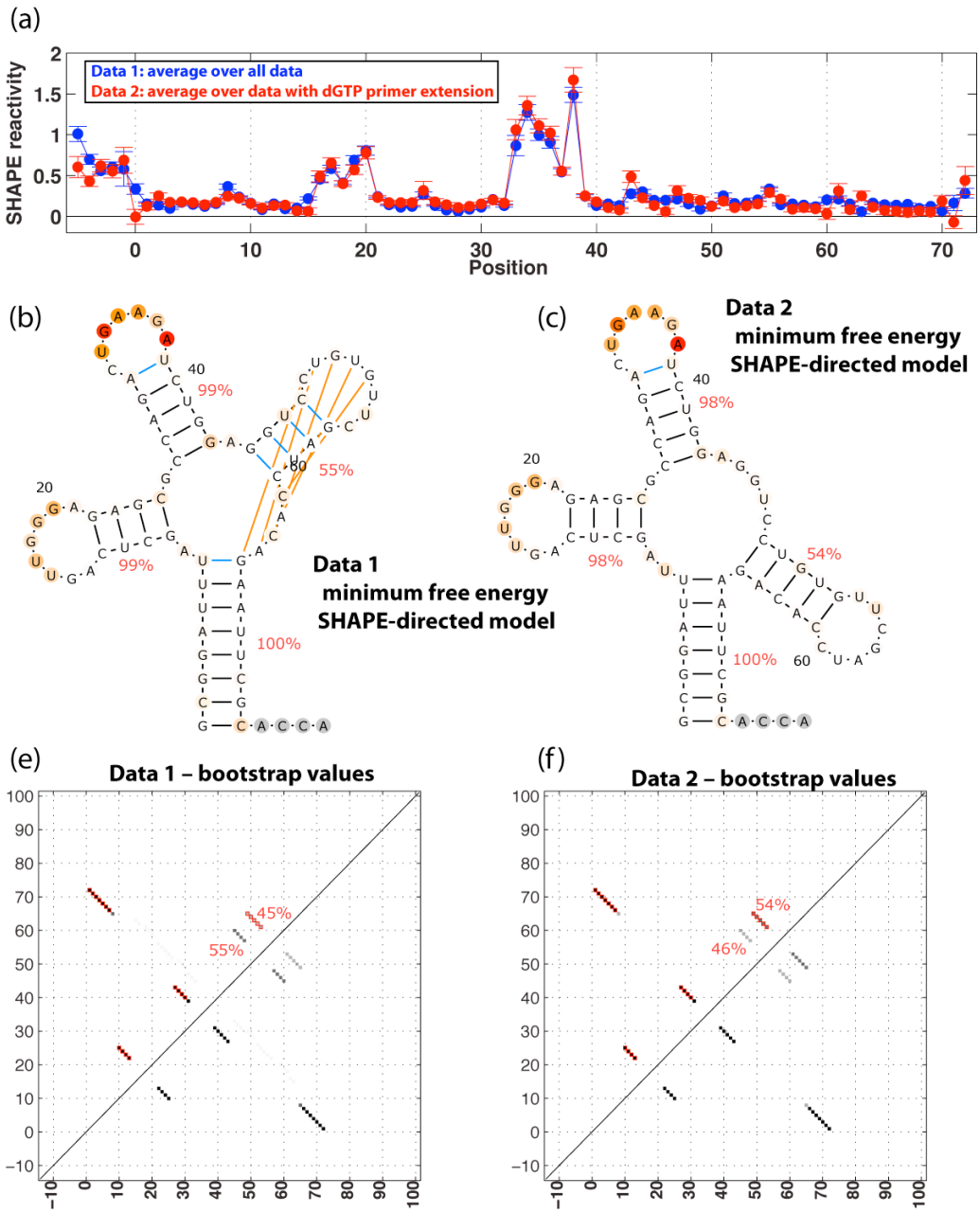

Figure S7. HIV-1 secondary structure helix confidence values compared to SHAPE reactivities. For each helix in the HIV-1 secondary structure model (*5*), the median SHAPE reactivity for nucleotides in the helix was computed, and plotted against bootstrap values. Blue line marks median reactivity over all nucleotides. High-bootstrap-value helices (e.g., four helices in TAR, three helices in gag-pol, and the gp120 signal-peptide stem; shown as red x's) typically have low median SHAPE reactivities. However, the converse is not true. Low-reactivity helices frequently have poor bootstrap values, indicating the existence of multiple secondary structures consistent with the data while still protecting the associated regions.

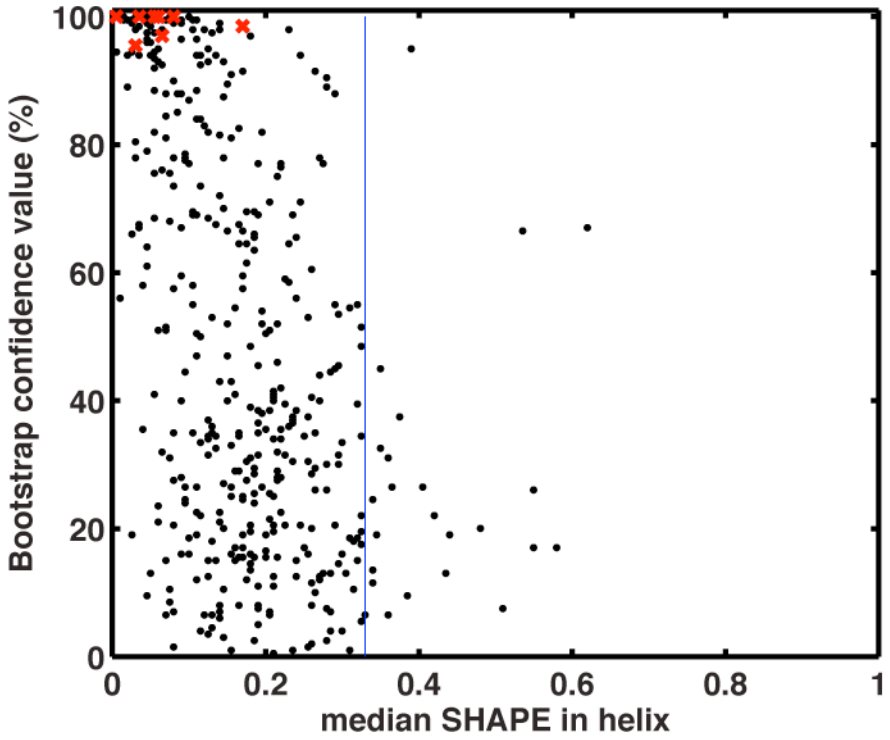

Figure S8. Histogram and fit of SHAPE reactivities. SHAPE reactivities of all residues for the six test RNAs (black; see SI Table S1), compared to least-squares fit (red) to a simple probability distribution P(x). The distribution was assumed to take the form P(x) = N exp($F_+|x-x_0|$) for $x > x_0$; and P(x) = N exp($F_-|x-x_0|$) for $x \leq x_0$. The presented fit is for $x_0 = 0.06$; $F_+ = 5.0$; $F_- = 25.0$.

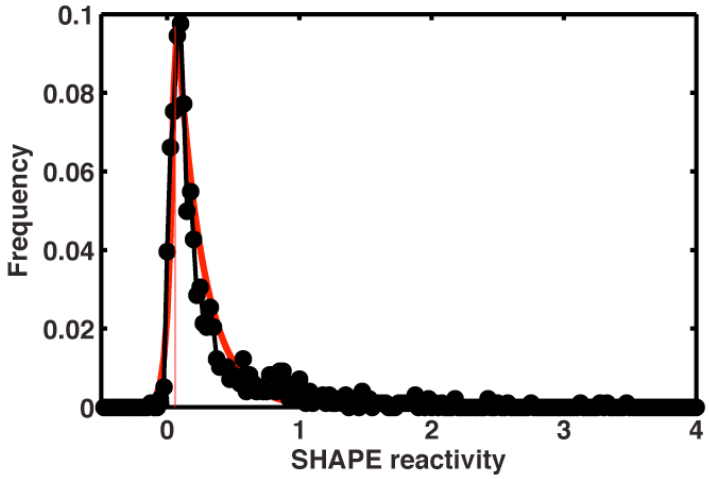

References for Supporting Information

1. Deigan, K. E., Li, T. W., Mathews, D. H., and Weeks, K. M. (2009) Accurate SHAPE-directed RNA structure determination, *Proc Natl Acad Sci U S A 106*, 97-102.
2. Vasa, S. M., Guex, N., Wilkinson, K. A., Weeks, K. M., and Giddings, M. C. (2008) ShapeFinder: a software system for high-throughput quantitative analysis of nucleic acid reactivity information resolved by capillary electrophoresis, *RNA 14*, 1979-1990.
3. Yoon, S. R., Kim, J., and Das, R. (2011) HiTRACE: High Throughput Robust Analysis of Capillary Electropherograms, *Bioinformatics*, in press.
4. Vicens, Q., Gooding, A. R., Laederach, A., and Cech, T. R. (2007) Local RNA structural changes induced by crystallization are revealed by SHAPE, *Rna 13*, 536-548.
5. Watts, J. M., Dang, K. K., Gorelick, R. J., Leonard, C. W., Bess, J. W., Jr., Swanstrom, R., Burch, C. L., and Weeks, K. M. (2009) Architecture and secondary structure of an entire HIV-1 RNA genome, *Nature 460*, 711-716.
6. Lukavsky, P. J. (2009) Structure and function of HCV IRES domains, *Virus Res 139*, 166-171.
7. Takamoto, K., Das, R., He, Q., Doniach, S., Brenowitz, M., Herschlag, D., and Chance, M. R. (2004) Principles of RNA compaction: insights from the equilibrium folding pathway of the P4-P6 RNA domain in monovalent cations, *Journal of Molecular Biology 343*, 1195-1206.
8. Correll, C. C., Freeborn, B., Moore, P. B., and Steitz, T. A. (1997) Metals, motifs, and recognition in the crystal structure of a 5S rRNA domain, *Cell 91*, 705-712.
9. Rieder, R., Lang, K., Graber, D., and Micura, R. (2007) Ligand-induced folding of the adenosine deaminase A-riboswitch and implications on riboswitch translational control, *Chembiochem 8*, 896-902.
10. Mulhbacher, J., Brouillette, E., Allard, M., Fortier, L. C., Malouin, F., and Lafontaine, D. A. (2010) Novel riboswitch ligand analogs as selective inhibitors of guanine-related metabolic pathways, *PLoS Pathog 6*, e1000865.
11. Smith, K. D., Lipchock, S. V., Livingston, A. L., Shanahan, C. A., and Strobel, S. A. (2010) Structural and biochemical determinants of ligand binding by the c-di-GMP riboswitch, *Biochemistry 49*, 7351-7359.
12. Kulshina, N., Baird, N. J., and Ferre-D'Amare, A. R. (2009) Recognition of the bacterial second messenger cyclic diguanylate by its cognate riboswitch, *Nature structural & molecular biology 16*, 1212-1217.
13. Kwon, M., and Strobel, S. A. (2008) Chemical basis of glycine riboswitch cooperativity, *RNA 14*, 25-34.